



Universiteit Utrecht



Faculteit Bètawetenschappen

# Testing alternative theories to General Relativity through lensed Gravitational Waves

BACHELOR THESIS

*J. Leon Kamermans*

Natuur- en Sterrenkunde

*Supervisors:*

dr. M.K. Haris

Institute for Gravitational and Subatomic Physics, Utrecht University

prof. dr. C. F. F. van den Broeck

Institute for Gravitational and Subatomic Physics, Utrecht University

16th June 2021

**Abstract**

Gravitational waves are ripples in space-time, generated by superheavy objects rotating around each other. These waves travel through space contain information about the objects which caused them, which can be retrieved when they are detected and analysed. The way in which these waves alter space-time are very distinct, up to six of these so called *polarisations* are possible. The number of these polarisations present in theories of gravity actually differ: if we would be able to measure how much exist, we could use this to validate these theories. When we use lensed gravitational waves, we would be able to do this with just 3 detectors. A framework is developed to allow for these waves to be combined and analysed, and simulations are ran as a proof of concept and demonstrate the workings of this framework.

# Contents

<b>1</b>	<b>Introduction</b>	<b>4</b>
<b>2</b>	<b>General Relativity and Gravitational Waves</b>	<b>5</b>
2.1	General Relativity in broad strokes . . . . .	5
2.2	Gravitational Waves and their observations . . . . .	6
2.3	Derivations in GR . . . . .	8
2.3.1	Geodesic Deviation and Tidal Force . . . . .	8
2.3.2	Linearised Einstein Equations . . . . .	10
2.3.3	Metric perturbations and wave properties in GR . . . . .	10
2.3.4	Effects of a gravitational wave on test particles . . . . .	11
<b>3</b>	<b>Gravitational Waves in Binary Inspiral</b>	<b>12</b>
3.1	The Energy of a gravitational wave . . . . .	12
3.2	Frequency and Phase Evolution . . . . .	13
3.3	Stationary Phase Approximation . . . . .	14
3.3.1	Validity of the SPA . . . . .	14
<b>4</b>	<b>Post Einsteinian theories of Gravity and their Waveforms</b>	<b>15</b>
4.1	Non-GR theories and polarisations . . . . .	15
4.2	Orientation of the detectors and measured signal . . . . .	17
4.3	Waveforms . . . . .	19
4.3.1	New parameters . . . . .	19
4.3.2	GR . . . . .	19
4.3.3	Brans-Dicke . . . . .	20
4.3.4	Rosen . . . . .	21
4.3.5	Lightman-Lee . . . . .	21
<b>5</b>	<b>Lensing of Gravitational Waves</b>	<b>22</b>
5.1	Basic Principles of Gravitational Lensing . . . . .	22
5.2	Effect on Gravitational Waveform . . . . .	25
5.3	Lensing rates . . . . .	26
<b>6</b>	<b>Model selection and Parameter Estimation</b>	<b>27</b>
6.1	Characteristics of the noise . . . . .	27
6.1.1	Cause of noise . . . . .	27
6.1.2	Power spectral density . . . . .	28
6.1.3	Gaussian noise . . . . .	28
6.1.4	Signal to Noise Ratio . . . . .	29
6.2	Bayes' theorem . . . . .	29
6.3	How to estimate parameters . . . . .	30
6.3.1	Nested sampling . . . . .	31
<b>7</b>	<b>Binary systems and Parameters</b>	<b>32</b>
7.1	Gravitational wave parameters . . . . .	33
7.2	Binary systems . . . . .	34
7.2.1	Binary Black Holes . . . . .	34
7.2.2	Neutron Star Black Hole . . . . .	34

<b>8</b>	<b>Results</b>	<b>35</b>
8.1	How the results are obtained . . . . .	35
8.2	Bayes factors . . . . .	35
8.3	Results per system . . . . .	36
8.3.1	Binary Black Hole . . . . .	36
8.3.2	Neutron Star Black Hole . . . . .	40
<b>9</b>	<b>Conclusion</b>	<b>43</b>
	<b>Acknowledgements</b>	<b>43</b>
	<b>References</b>	<b>44</b>
<b>A</b>	<b>Appendix</b>	<b>47</b>

# 1 Introduction

In 1905, Albert Einstein published his groundbreaking *Zur Elektrodynamik bewegter Körper*, in which he showed the principles of special relativity. This theory does not hold true for non-inertial systems, and thus a more general theory had to be developed to incorporate gravity. In 1916, he published *Die Grundlage der allgemeinen Relativitätstheorie*, where he gave his famous equations now known as the *Einstein field equations*[1]. A very interesting consequence of General Relativity are *gravitational waves*. In 1916, Albert Einstein published *Näherungsweise Integration der Feldgleichungen der Gravitation*[2], in which he postulates their existence. When to supermassive objects, say two black holes, rotate around each other, their gravitational pull is so large that they distort space-time itself. We can measure these distortions using gigantic detectors, as space itself extends and contracts. These ripples in space-time, much like the ripples of a pond when we throw a stone in it, travel through the universe from their point of origin all the way to the earth.

However, Einstein also saw that the effects of these waves would be so minuscule that they would probably never be detected[3]. However, this turned out not to be the case, as in september 2015, the first gravitational waves were ever detected by the LIGO/Virgo collaboration, an event known as GW150914[4]. The two LIGO (Laser Interferometer Gravitational-Wave Observatory) detectors at Hanford and Livingston, USA, detected the same gravitational wave with a time difference of about 7 milliseconds. In 2017, the Nobel Prize in Physics was awarded to Rainer Weiss, Barry C. Barish and Kip Thorne "for decisive contributions to the LIGO detector and the observation of gravitational waves"[5].

General relativity however is not the only theory of gravity, albeit the most accepted one. Other ones include the Brans-Dicke [6], Lightman-Lee [7] and Rosen [8][9] theories of gravity. Since most theories produce their own distinct gravitational waves, their detection can be used to look at their validity. One very distinct difference between General Relativity and other theories of gravity are the number of so called *polarisations*: unique directions in which space-time is distorted by the gravitational wave. In General Relativity, there are two, but there can be up to six in different theories. In order to measure each of these polarisations individually, we need at least as many detectors as polarisations present in the gravitational wave [10].

While there are not yet 6 gravitational wave detectors, we can use a network of 3 detectors to measure the same wave 6 times using gravitational lensing [10]. Gravitational wave lensing occurs when a very heavy object (such as a black hole or even an entire galaxy) distorts and curves space-time around it, altering the trajectory of a gravitational wave in such a way that the same wave arrives at our detectors twice, at different times [11] [12]. Since the detectors have a different orientation between the first and second observation of the wave due to the rotation of the earth, we effectively have a network of 6 detectors.

For the thesis, a framework was developed to allow for the simultaneous analysis of the two detections of the same gravitational wave with the goal of looking into the different polarisations present in a gravitational wave. As a proof of concept and workings of this framework, we will be simulating gravitational waves for the theories of General Relativity, Brans-Dicke, Lightman-Lee and Rosen, after which we look into how well the framework can distinguish between the different theories.

## 2 General Relativity and Gravitational Waves

In this chapter, we will take a look at Einstein's theory of General relativity and its fundamental equations in section 2.1. In section 2.2, we take a look at the fundamentals of gravitational waves and how they are detected. We continue in section 2.3, where we derive some of the most important equations of General Relativity that are used in gravitational waves. In this thesis, Einstein's summation convention is used. When the same index is used twice as both an upper and lower index, a summation over that index is implied. Or, in formula form:

$$A_\alpha B^\alpha = \sum_\alpha A_\alpha B^\alpha.$$

We also use a geometrized unit system, which means that we take Newton's constant of gravity and the speed of light to be equal to unity, or

$$G = c = 1.$$

### 2.1 General Relativity in broad strokes

In 1916, Einstein published *Die Grundlage der allgemeinen Relativitätstheorie*, where he gave his famous equations now known as the *Einstein field equations*, where he laid the foundations for General Relativity [1]. Here we will a slightly different and more modern representation as given in equation (8.7) of [13], where the field equations take the form

$$G^{\alpha\beta} + \Lambda g^{\alpha\beta} = 8\pi T^{\alpha\beta}, \quad (2.1)$$

where  $G^{\alpha\beta}$  is the *Einstein tensor*,  $g^{\alpha\beta}$  is the *metric tensor*,  $\Lambda$  is the cosmological constant and  $T$  is the stress-energy tensor. The cosmological constant  $\Lambda$  contains information about the rate of expansion of the universe: if positive, the expansion accelerates [14]. It can be shown that this combination of  $\Lambda g^{\alpha\beta}$  is of no influence on the final equations we will be deriving, so for the rest of the paper we take  $\Lambda = 0$  [13]. The metric tensor  $g_{\alpha\beta}$  contains the information of space-time which is used to measure the distance in space-time between two points (equation 1.1 of [15])

$$ds^2 = g_{\mu\nu} dx^\mu dx^\nu, \quad (2.2)$$

where  $x^\mu$  is a four vector which contains the time and spatial components of the point.

$G_{\alpha\beta}$  contains information about the curvature of space-time, and is related to the so called *Riemann tensor*, another tensor which contains information about the curvature of space-time via the relation (combining equations 6.98, 6.91 and 6.92 from [13]):

$$G_{\alpha\beta} = R^\mu_{\alpha\mu\beta} - \frac{1}{2} g_{\alpha\beta} g^{\mu\nu} g^{\gamma\sigma} R_{\mu\nu\gamma\sigma}. \quad (2.3)$$

Here,  $R^\alpha_{\mu\nu\beta}$  is the Riemann tensor, and is defined as (equation 1.8 of [15])

$$R^\alpha_{\mu\nu\beta} = \frac{\partial}{\partial x^\nu} \Gamma^\alpha_{\mu\beta} - \frac{\partial}{\partial x^\beta} \Gamma^\alpha_{\mu\nu} + \Gamma^\alpha_{\nu\rho} \Gamma^\rho_{\mu\beta} - \Gamma^\alpha_{\beta\rho} \Gamma^\rho_{\mu\nu}, \quad (2.4)$$

with  $\Gamma^\mu_{\alpha\beta}$  the *Christoffel symbol*, as defined in equation (1.5) of [15]:

$$\Gamma^\mu_{\alpha\beta} = \frac{1}{2} g^{\mu\gamma} \left( \frac{\partial}{\partial x^\beta} g_{\alpha\gamma} + \frac{\partial}{\partial x^\alpha} g_{\beta\gamma} - \frac{\partial}{\partial x^\gamma} g_{\alpha\beta} \right). \quad (2.5)$$

A special case of the metric tensor  $g_{\mu\nu}$  is when there is gravity present, i.e. a perfect vacuum with no external gravitational fields, when the metric tensor is just the *Minkowski metric*  $\eta_{\mu\nu}$ :

$$\eta_{\mu\nu} = \begin{pmatrix} -1 & 0 & 0 & 0 \\ 0 & 1 & 0 & 0 \\ 0 & 0 & 1 & 0 \\ 0 & 0 & 0 & 1 \end{pmatrix} \quad (2.6)$$

It easily follows from the above equation that in this case,  $ds^2 = dx^2 + dy^2 + dz^2 - d\tau^2$ , as we would expect in the non-relativistic case.

The first non-trivial solution for  $g_{\mu\nu}$  was found by Karl Schwarzschild in 1916. The so called *Schwarzschildmetric* describes space around a point mass, and is given by [16]

$$d\tau^2 = \left(1 - \frac{r_s}{r}\right) dt^2 - \frac{dr^2}{1 - \frac{r_s}{r}} - r^2(d\theta^2 + \sin^2 \theta d\phi^2),$$

where  $r$ ,  $\phi$  and  $\theta$  are the standard spherical coordinates, and  $r_s$  is the so-called *Schwarzschild radius*, which is given by  $r_s = 2M$ . A very interesting consequence of this metric are black holes, which will be treated later in this thesis.

## 2.2 Gravitational Waves and their observations

See also figure **INSERT FIGURE ONE FROM [4]**. Below in figure 1, a schematic representation of the interferometers which are used in gravitational wave detections is given. Very crudely said, they are traditional Michelson interferometers, blown up to gigantic scales: the Japanese KAGRA detector has arms of nearly 3 kilometres long, and the LIGO detectors are nearly 4 kilometres long. When a gravitational wave goes through the detector, space-time within the detector is distorted, resulting in the fact that the length of the arms of the detectors change. How exactly the shape of space-time changes is derived later in this chapter: as we will show, the length of the two detector arms will differ through this. A laser is shot into the two arms using a beam splitter which reflects half of the light into one arm, and the other half into the other. The two bundles reflect at the end of their arms, and are sent back at the beam splitter, where they are recombined. Due to the difference in arm length, the bundles arrive with a different phase, which then leads to interference of the amplitude of the combined laserbeam[17]. This is measured at the photodetector at the end of the interferometer, from which we know the difference in length of the two arms. This difference is absurdly small: the LIGO detectors are able to measure a difference in length of  $1/10.000$  of the radius of a proton of their 4 kilometre long arms [18]. This is equivalent to the width of a hair over the distance between us and the nearest star system *Proxima Centauri*, 4.2 lightyears away.

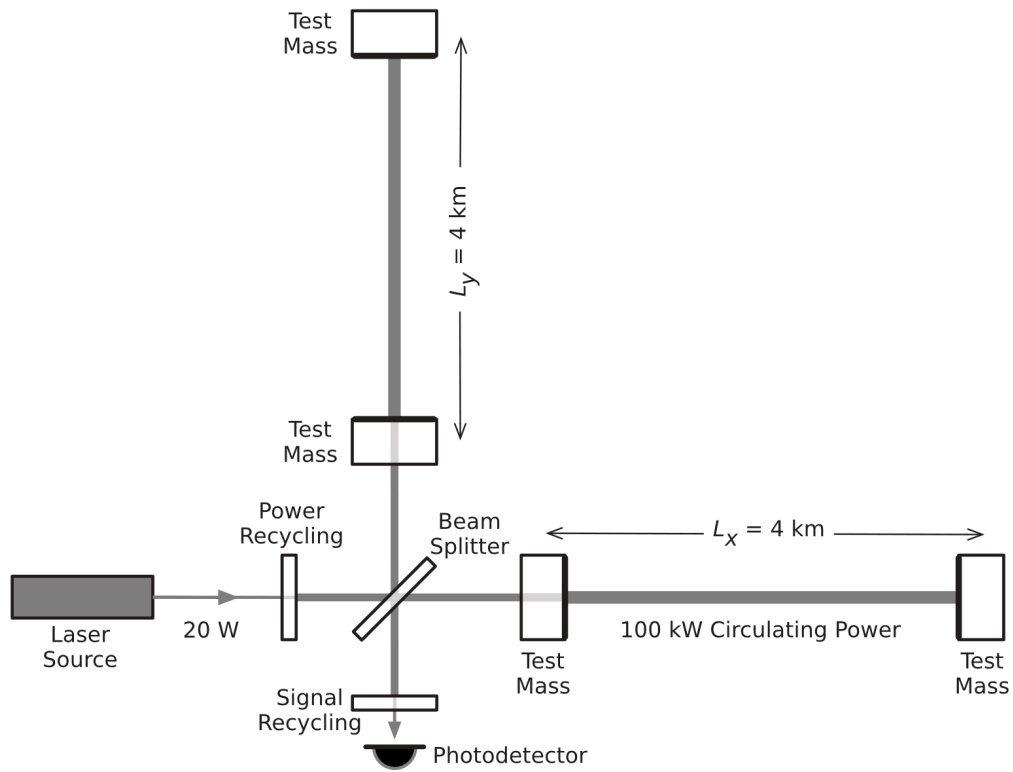


Figure 1: A schematic not-to-scale representation of a laser interferometer, specifically the LIGO detectors. Adapted from figure 2 of [4].

The detectors mostly recover only noise, which is created by thermal or mechanical vibrations in the detectors. Because of this, an event has to be found in multiple detectors around the world to make sure that the wave event is no statistical fluke of the noise. During this thesis, we will be using (virtual instances of) three detectors: LIGO Hanford, LIGO Livingston and KAGRA. Their relevant statistics and characteristics are defined in the *bilby* package [19], which is used throughout the project.



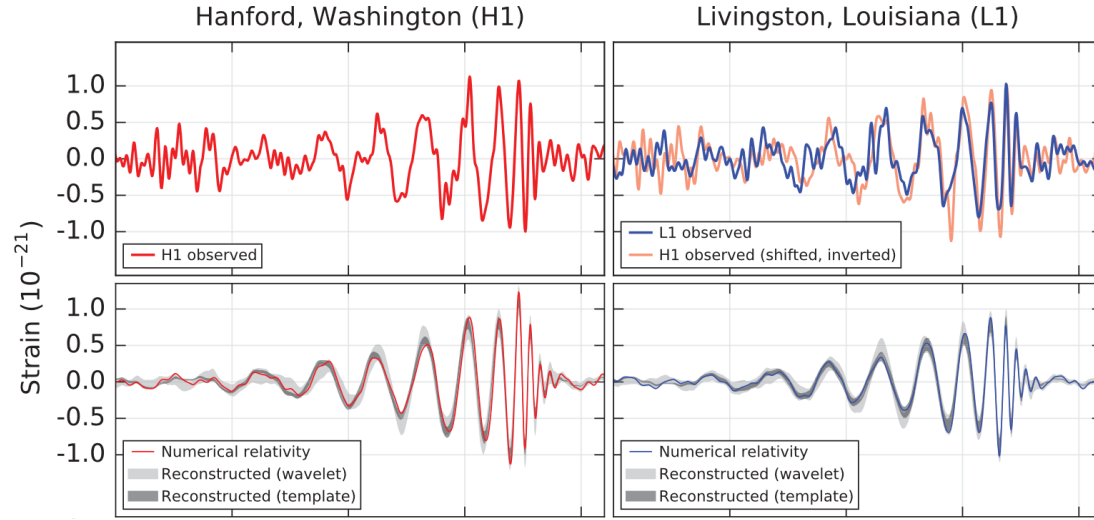


Figure 2: The first gravitational wave event, GW150914 as observed in the LIGO Hanford (H1) and LIGO Livingston (L1) detectors. Top left: the measured strain in the H1 detector. Top right: the measured strain of in the L1, with the H1 measured strain superimposed over it. Bottom left: in red the reconstructed waveform from H1 the using numerical relativity, with in grey the 90% credibility region. Bottom right: in red the reconstructed waveform from L1 the using numerical relativity, with in grey the 90% credibility region. Adapted from figure 2 of [4].

## 2.3 Derivations in GR

### 2.3.1 Geodesic Deviation and Tidal Force

In an Euclidean space, two straight lines that start parallel to each other will stay parallel, no matter their length. We call the space-time geometry of such models *flat space-time*, and their metric is given by the Minkowski metric as defined in equation 2.6[13]. This seems to be the case for the world we observe around us, and holds true in Newtonian physics. However, when our world is exposed to strong nonuniform gravitational fields, this assumption does not hold: parallel straight lines do not stay parallel under these circumstances when they are stretched enough. The geometry of such non-Euclidean space-times are called *curved space-time*.

The space-time of GR (and all other alternative theories which will be discussed here) are Riemannian spaces. This means that space-time is flat when we look at a sufficiently small portion of it, but becomes curved when we start to zoom out. A very practical application of this are two particles which are both freely falling in a gravitational field, produced by an object very far away. They will both be falling in straight lines, which are parallel to each other, and keep following these straight lines. In the beginning they will fall parallel to each other, but over a longer portion of time their straight paths are no longer parallel to each other. The paths of such falling particles are called *geodesics*.

The path the particles follow on these geodesics is called the geodesic equation, and defined

in equation (6.51) in [13] as

$$\frac{d}{d\lambda} \left( \frac{dx^\alpha}{d\lambda} \right) + \Gamma_{\mu\beta}^\alpha \frac{dx^\mu}{d\lambda} \frac{dx^\beta}{d\lambda} = 0,$$

with  $\Gamma_{\alpha\beta}^\mu$  the Christoffel symbol as defined in equation 2.5. If we take two particles which are freely falling, we can connect them via a vector  $\vec{\xi}$ , a four-vector which contains the proper time difference  $\xi^0$  and proper distances between the two. The evolution of component  $\xi^\alpha$  is derived in Schutz (equation 9.25 from [13]) to be

$$\frac{d^2}{d\tau^2} \xi^\alpha = R_{\mu\nu\beta}^\alpha U^\mu U^\nu \xi^\beta,$$

where  $\vec{U} = d\vec{x}/d\tau$  is the four-velocity of the particles, where  $x^0 = \tau$  is the time component, and  $x^1, x^2, x^3$  are the three spatial components, and  $R_{\mu\nu\beta}^\alpha$  is the Riemann-tensor as defined in equation 2.4. If we now impose the initial condition that the particles are stationary with respect to each other, so  $\vec{U} = (1, 0, 0, 0)$ , we obtain that

$$\frac{d^2}{d\tau^2} \xi^\alpha = R_{00\beta}^\alpha \xi^\beta = -R_{0\beta 0}^\alpha \xi^\beta. \quad (2.7)$$

The result above is called the *tidal force* of the gravitational wave: when it changes the shape of the space around the two particles, the proper distance between them starts to change, as if they are moved by a force. Equation 2.7 holds true for all metric theories of gravity, and thus for all theories of gravity which are treated in this thesis.

The following procedures follow section 6.5 of [13]. In order to find how the gravitational waves enter equation 2.7, we first express the Riemann tensor in terms of the space-time metric  $g$  as defined in equation 2.4. Using equation 2.5, and using that the space is locally flat, we obtain that for a point in a local inertial frame  $\Gamma_{\alpha\beta}^\mu = 0$ , but its derivative is equal to

$$\frac{\partial}{\partial x^\sigma} \Gamma_{\alpha\beta}^\mu = \frac{1}{2} g^{\mu\gamma} \left( \frac{\partial^2}{\partial x^\sigma \partial x^\beta} g_{\alpha\gamma} + \frac{\partial^2}{\partial x^\sigma \partial x^\alpha} g_{\beta\gamma} - \frac{\partial^2}{\partial x^\sigma \partial x^\gamma} g_{\alpha\beta} \right).$$

If we substitute this into equation 2.4, we obtain that

$$\begin{aligned} R_{\mu\nu\beta}^\alpha &= \frac{1}{2} g^{\alpha\sigma} \left( \frac{\partial^2}{\partial x^\beta \partial x^\nu} g_{\sigma\mu} + \frac{\partial^2}{\partial x^\mu \partial x^\nu} g_{\sigma\beta} - \frac{\partial^2}{\partial x^\sigma \partial x^\nu} g_{\mu\beta} - \frac{\partial^2}{\partial x^\nu \partial x^\beta} g_{\sigma\mu} - \frac{\partial^2}{\partial x^\mu \partial x^\beta} g_{\sigma\nu} + \frac{\partial^2}{\partial x^\sigma \partial x^\beta} g_{\mu\nu} \right) \\ &= \frac{1}{2} g^{\alpha\sigma} \left( \frac{\partial^2}{\partial x^\mu \partial x^\nu} g_{\sigma\beta} - \frac{\partial^2}{\partial x^\sigma \partial x^\nu} g_{\mu\beta} - \frac{\partial^2}{\partial x^\mu \partial x^\beta} g_{\sigma\nu} + \frac{\partial^2}{\partial x^\sigma \partial x^\beta} g_{\mu\nu} \right), \end{aligned} \quad (2.8)$$

where we used the commutativity of partial derivatives.

Following section 8.3 of [13], we approximate that for weak gravitational fields, where space-time is nearly flat, the space-time metric is equal to the flat Minkowski metric  $\eta$  with a metric perturbation  $h$ . We thus write that

$$g_{\alpha\beta} = \eta_{\alpha\beta} + h_{\alpha\beta},$$

with  $|h_{\alpha\beta}| \ll 1$ . Since we know from equation 2.6 that the derivatives of the Minkowski metric vanish, we can substitute the above into equation 2.8, perform some simple algebra and discard the higher order terms to obtain that

$$R_{\alpha\mu\nu\beta} = \frac{1}{2} \left( \frac{\partial^2}{\partial x^\mu \partial x^\nu} h_{\alpha\beta} + \frac{\partial^2}{\partial x^\alpha \partial x^\beta} h_{\mu\nu} - \frac{\partial^2}{\partial x^\mu \partial x^\beta} h_{\alpha\nu} - \frac{\partial^2}{\partial x^\alpha \partial x^\nu} h_{\mu\beta} \right), \quad (2.9)$$

which is the Riemann tensor written in terms of the linear metric perturbation. This can be substituted back into equation 2.7 to obtain the tidal force, and thus movement of particles, in terms of the metric perturbation  $h$ .

### 2.3.2 Linearised Einstein Equations

In the following sections, we will explore how we can use the expressions as given above to see how gravitational waves deform space in GR. Using the result from equation 2.9, we can rewrite the Einstein field equations as defined in equation 2.1. We can rewrite the metric perturbation  $h$  as *trace reversed metric perturbation* as given in equation (1.12) of [15],

$$\bar{h}_{\alpha\beta} \equiv h_{\alpha\beta} - \frac{1}{2}h_{\gamma}^{\gamma}g_{\alpha\beta}.$$

If we substitute the above into equation 2.9 and equation 2.10, we obtain that the Einstein tensor is equal to (equation (1.13))

$$G_{\mu\nu} = -\frac{1}{2} \left( \frac{\partial^2}{\partial x^\alpha \partial x_\mu} \bar{h}_{\nu\alpha} + \frac{\partial^2}{\partial x^\alpha \partial x_\nu} \bar{h}_{\mu\alpha} - \frac{\partial^2}{\partial x^\alpha \partial x_\alpha} \bar{h}_{\mu\nu} - \eta_{\mu\nu} \frac{\partial^2}{\partial x^\alpha \partial x_\beta} \bar{h}_{\alpha\beta} \right). \quad (2.10)$$

The gauge transformation, a transformation which leaves the Riemann tensor invariant, of  $\bar{h}$  is given by

$$\bar{h}'_{\mu\nu} = \bar{h}_{\mu\nu} - \frac{\partial}{\partial x_\mu} \zeta_\nu - \frac{\partial}{\partial x_\nu} \zeta_\mu + \eta_{\mu\nu} \frac{\partial}{\partial x^\alpha} \zeta_\alpha.$$

We can easily simplify equation 2.10 if we set the so called *Lorentz gauge condition* (equation 8.33 of [13]):

$$\frac{\partial}{\partial x_\nu} \bar{h}^{\mu\nu} = 0. \quad (2.11)$$

Using both this, equation 2.10 and the *D'Alembertian*, or four-dimensional Laplacian, as defined in equation (8.37) of [13] as

$$\square f = \left( -\frac{\partial^2}{\partial t^2} + \nabla^2 \right) f = \frac{\partial^2}{\partial x^\alpha \partial x_\alpha} f = \eta^{\alpha\beta} \frac{\partial^2}{\partial x_\alpha \partial x_\beta} f,$$

the Einstein field equations (equation 2.1) reduce to:

$$\square \bar{h}_{\mu\nu} = -16\pi T_{\mu\nu}. \quad (2.12)$$

This set of equations are called the *Linearised Einstein equations*, since all terms are linear, and are valid for weak gravitational fields.

### 2.3.3 Metric perturbations and wave properties in GR

In this section, we will follow chapter 9.1 from Schutz [13]. The stress-energy tensor  $T_{\mu\nu}$  of equation 2.12 is completely empty when we consider a perfect vacuum with no electromagnetic fields present. In this case, equation 2.12 thus reduces to

$$\square \bar{h}_{\mu\nu} = 0.$$

The solutions to this equation are given by

$$\bar{h}_{\mu\nu} = A_{\mu\nu} e^{ik_\alpha x^\alpha}, \quad (2.13)$$

where it can be shown that this solution holds if  $k^\alpha k_\alpha = 0$ , or that  $k^\alpha$  is a null vector. We can expand the exponent of equation 2.13 to be equal to

$$k_\alpha x^\alpha = \omega t + \vec{k} \cdot \vec{x},$$

where  $\omega = k_0$  is the frequency of the wave, and  $\vec{k}$  is the direction of propagation. Since  $k^\alpha$  is a null vector, it follows that  $|\vec{k}|^2 = \omega^2$ , from which it follows that the phase velocity of the wave[17] is equal to  $\omega/k = 1$ , and that gravitational waves thus show no dispersion.

We can also now derive the velocity of the gravitational wave. If we take a photon which travels in the same direction as vector  $\vec{k}$ , we can write its position with regards to the wave as

$$x^\mu(\lambda) = k^\mu \lambda + l^\mu,$$

where  $\lambda$  is some parameter and  $l$  the initial distance between the photon and wave at  $\lambda = 0$ . If we multiply each side with  $k_\mu$  and use the fact that  $k_\mu k^\mu = 0$ , we obtain that

$$k_\mu x^\mu(\lambda) = k_\mu l^\mu,$$

and thus that the separation is constant. We have thus shown that gravitational waves follow the exact path of photons with the speed of light in GR. Note that this is not true for all theories, such as Rosen, where there is a difference in velocity between light and gravitational waves[20].

### 2.3.4 Effects of a gravitational wave on test particles

The matrix  $A$  from equation 2.13 has the dimensions 4x4, but we can simplify this further in GR by imposing something called the *transverse traceless gauge*, which we will show now. We already used the *Lorentz gauge*, so using equation 2.11 it follows that

$$A^{\alpha\beta} k_\beta = 0,$$

or that  $A$  is completely orthogonal to the direction of motion of the gravitational wave in GR. If we take the very simple assumption that our wave travels along the  $z$ -axis, that all components  $A_{\alpha\beta}$  with either  $\alpha$  or  $\beta$  equal to  $z$  are empty. It can be shown that there are two more conditions which can be put upon  $A$ , the first being

$$A_{\alpha\beta} U^\beta = 0.$$

It can be shown that we may take  $U^\beta = \delta_0^\beta$ , with  $\delta$  the Kronecker delta, which results in all the terms with an index 0 of  $A$  are empty. If we finally take the final condition

$$A^\alpha_\alpha = 0,$$

which can be shown by some algebra, we know that  $A$  can be represented as

$$A_{\alpha\beta}^{TT} = \begin{pmatrix} A_{xx} & A_{xy} & 0 \\ A_{xy} & -A_{xx} & 0 \\ 0 & 0 & 0 \end{pmatrix}, \quad (2.14)$$

This equation we used that  $A^{TT}$  is symmetrical and we removed the indices using time for simplicity (since they are all 0). Within the transverse traceless gauge, we have thus 2 distinct ways at which spacetime is being warped by the gravitational waves. If we substitute equation 2.14

into equation 2.13, relate  $\bar{h}_{\mu\nu}$  to the Riemann tensor  $R$  using equation 2.9 and insert that into the tidal force of equation 2.7, we obtain the equations of motions of two particles which the gravitational wave goes through. It can easily be shown that two particles separated in the x-direction by a distance  $\epsilon$  with vector  $\vec{\xi}$  move as

$$\frac{\partial^2}{\partial t^2}\xi^x = \frac{1}{2}\epsilon \frac{\partial^2}{\partial t^2}h_{xx}^{TT}, \quad \frac{\partial^2}{\partial t^2}\xi^y = \frac{1}{2}\epsilon \frac{\partial^2}{\partial t^2}h_{xy}^{TT}.$$

When the particles are only separated in the y-direction by a distance  $\epsilon$ , the vector  $\vec{\xi}$  connecting the two changes as

$$\frac{\partial^2}{\partial t^2}\xi^x = \frac{1}{2}\epsilon \frac{\partial^2}{\partial t^2}h_{xy}^{TT}, \quad \frac{\partial^2}{\partial t^2}\xi^y = -\frac{1}{2}\epsilon \frac{\partial^2}{\partial t^2}h_{xx}^{TT}.$$

We can visualise these equations of motion using a ring of test particles. From now on, we will use the naming convention that  $h_{xx} = h_+$  and  $h_{xy} = h_\times$ , due to reasons which will be presented in the next section. We call  $A_{\alpha\beta}$  the *polarisation tensor*, and every of its unique components a *polarisation mode*. These modes directly determine the way that a gravitational wave distorts space.

### 3 Gravitational Waves in Binary Inspiral

In the previous section, we laid the foundations of how gravitational waves distort space-time. In this section, we will derive the shape of a gravitational wave that is generated by two massive objects spiralling towards each other before ultimately colliding. This is also called the *inspiral*. In section 3.1, we derive just how much energy enters a gravitational wave every second by relating it to the orbital energy of the two spiralling objects. Then, in section 3.2, we derive the frequency and phase of the gravitational waves. Finally, in section 3.3 we discuss the Stationary Phase Approximation, a crucial approximation used when deriving gravitational waves, and take a look at previous research concerning its accuracy.

#### 3.1 The Energy of a gravitational wave

During this section until stated otherwise, we will follow [21]. When two massive objects circle around each other, they emit gravitational waves. Of course, energy is conserved, and thus this energy must come from somewhere. As a result of the gravitational waves, the orbital energy of the two objects decreases by an equal amount as is put into the gravitational wave. In equation form, we can write this as

$$\frac{dE_{\text{orb}}}{dt} = -\frac{dE_{\text{GW}}}{dt}. \quad (3.1)$$

We can write the orbital energy as a linear sum of the kinetic and gravitational energy of the two objects, namely

$$E_{\text{orb}} = \frac{1}{2}mv_1^2 + \frac{1}{2}mv_2^2 - \frac{m_1m_2}{R},$$

where  $R$  is the distance between the two massive objects. It can be shown that  $v_1 = m_2 R \omega_1 / (m_1 + m_2)$  and  $v_2 = m_1 R \omega_1 / (m_1 + m_2)$ , where  $\omega$  is the orbital frequency. If we use this and combine this with Kepler's third law  $R^3 = M/\omega^2$  where  $M$  is the total mass, we can rewrite the orbital energy as

$$E_{\text{orb}} = -\frac{1}{2}\mathcal{M}^{5/3}\omega^{2/3}, \quad (3.2)$$

where  $\mathcal{M}$  is the *chirp mass*, which is a combination of the two masses given by

$$\mathcal{M} = \frac{(m_1 m_2)^{3/5}}{(m_1 + m_2)^{1/5}}. \quad (3.3)$$

Meanwhile, we can write the change in orbital energy as the change of orbital energy passing through a sphere which fully encloses the two circling objects. It can be shown that we can write this in terms of the entries in the  $h_{ij}$  matrix of equation 2.14, namely **EQUATION 3.31 & 3.32**

$$\frac{dE_{\text{GW}}}{dt} = \frac{r^2}{32\pi} \int \int \langle \dot{h}_{ij} \dot{h}_{ij} \rangle d\Omega = \frac{32}{5} (\mathcal{M}\omega)^{10/3} \quad (3.4)$$

where  $d\Omega = \sin \theta d\theta d\phi$ .

### 3.2 Frequency and Phase Evolution

If we insert equation 3.2 and 3.4 into 3.1, and define the *gravitational wave frequency*  $f_{\text{gw}} = \pi\omega$ , we obtain a differential equation for  $f_{\text{gw}}$ :

$$\frac{df_{\text{gw}}}{dt} = \frac{96}{5} \pi^{8/3} \mathcal{M}^{5/3} f_{\text{gw}}^{11/3}. \quad (3.5)$$

If we solve this equation, we obtain the gravitational wave frequency as a function of time:

$$f_{\text{gw}}(t) = \frac{1}{\pi} \mathcal{M}^{-5/8} \left( \frac{5}{256\tau(t)} \right)^{3/8}, \quad (3.6)$$

where  $\tau(t) = t_c - t$ , with  $t_c$  the so called *time of coalescence*. This is the time at which the two objects collide with each other, and  $f_{\text{gw}} \rightarrow \infty$ . This is of course a unphysical result, so there must be a maximum frequency.

It can be shown that there exists a so called *innermost stable circular orbit*, the smallest radius for which the inspiral can be described using quasi-circles. Below this radius, the two objects start to fall to each other and merge. This is also the point where to good approximation the generation of gravitational waves stops, so this is the upper limit to  $f_{\text{gw}}$ . If we use Kepler's third law to convert the radius to a frequency, we find that  $f_{\text{gw,ISCO}}$  is given by

$$f_{\text{gw,ISCO}} = \frac{1}{6^{3/2} \pi M}.$$

The phase of the gravitational wave  $\Phi_{\text{gw}}$  is directly related to the rate at which the two massive objects in inspiral rotate around each other, and thus  $f_{\text{gw}}$  via

$$2\pi f_{\text{gw}} = \dot{\Phi}_{\text{gw}}. \quad (3.7)$$

Integrating this equation yields the phase as a function of time:

$$\Phi_{\text{gw}}(t) = -2 \left( \frac{\tau(t)}{5\mathcal{M}} \right)^{5/8} + \Phi_c,$$

where  $\Phi_c$  is the phase at the time of coalescence .

### 3.3 Stationary Phase Approximation

In this section, we will follow procedures as set out in section I C of Cutler and Flanagan [22].

Right now, our frequencies and phase depend on time. However, we want a final function for the gravitational wave in terms of frequency. If we take  $h(t)$  to be our gravitational wave, we can use a Fourier transform to go to a gravitational wave dependant on the gravitational wave frequency  $\tilde{h}(f_{\text{gw}})$ , where the tilde indicates a Fourier transform. The formula for a Fourier transform of  $h(t)$  is given by

$$\tilde{h}(f_{\text{gw}}) = \int h(t) e^{2\pi i f t} dt. \quad (3.8)$$

If we make the assumption that we can write  $h(t)$  as a wave of the form  $h(t) = \mathcal{A}(t) \cos(\Phi_{\text{gw}}(t))$  with amplitude  $\mathcal{A}$  and phase  $\phi$ , we can rewrite the above equation by expanding the cosine into

$$\tilde{h}(f_{\text{gw}}) = \frac{1}{2} \int \mathcal{A}(t) \left( e^{2\pi i f_{\text{gw}} t + i \Phi_{\text{gw}}(t)} + e^{2\pi i f_{\text{gw}} t - i \Phi_{\text{gw}}(t)} \right) dt.$$

As stated in section I B of [23], there exists no value of  $t$  for which the argument of the left exponent in the brackets vanishes. Thus, via the Riemann-Lebesgue Lemma, its Fourier transform goes to zero as  $|t| \rightarrow \infty$ , and can thus be neglected.

The Fourier integral above cannot be solved analytically unless some approximation is used. The stationary phase approximation states that the largest contribution of the remaining integral comes from the *stationary point*, where the derivative of the exponent is zero, or  $\dot{\Phi}(t_s) = 2\pi f_{\text{gw}}$ . This time  $t_s(f_{\text{gw}})$  is not a scalar, but different for every frequency. If we Taylor expand around this point  $t_s(f)$ , we obtain that:

$$\tilde{h}_{\text{spa}}(f_{\text{gw}}) = \frac{1}{2} \int \mathcal{A}(t) e^{2\pi i f_{\text{gw}} t_s(f_{\text{gw}}) - i \Phi_{\text{gw}}(t_s(f_{\text{gw}})) - \frac{1}{2} i \ddot{\Phi}_{\text{gw}}(t_s(f_{\text{gw}})) (t - t_s(f_{\text{gw}}))^2} dt. \quad (3.9)$$

From equations 3.5 and 3.7, we can derive that

$$\begin{aligned} t_s(f_{\text{gw}}) &= t_c - 5(8\pi f_{\text{gw}})^{-8/3} \mathcal{M}^{-5/3} \\ \Phi_{\text{gw}}(t_s) &= \Phi(t_c) - 2(8\pi \mathcal{M} f_{\text{gw}})^{-5/3}, \end{aligned}$$

and we know that  $\ddot{\Phi}_{\text{gw}}(t) = 2\pi \dot{f}_{\text{gw}} = \frac{96}{5} \pi^{8/3} \mathcal{M}^{5/3} f_{\text{gw}}^{11/3}$ . If we then combine all of the above, insert it into equation 3.9, we obtain that

$$\tilde{h}_{\text{spa}}(f_{\text{gw}}) = \frac{\pi \mathcal{M}}{2} \mathcal{A}(t_c) (\pi \mathcal{M} f_{\text{gw}})^{-11/6} e^{i\psi},$$

with  $\psi$  the phase given by

$$2\pi f_{\text{gw}} t_c - \Phi_{\text{gw}}(t_c) - \frac{\pi}{4} + \frac{3}{256} (\pi \mathcal{M} f_{\text{gw}})^{-5/3}$$

#### 3.3.1 Validity of the SPA

It is of interest how accurate this SPA is. Droz *et al.* have shown very convincingly that this SPA is a very good approximation by deriving the leading order correction term for  $\tilde{h}_{\text{spa}}$ . From equations (2.23) and (2.26) of [24], this is taken to be

$$\tilde{h}_{\text{lo}}(f) = \tilde{h}_{\text{spa}}(f) (1 + \delta \mathcal{A}_w) e^{i(\delta\psi + \delta\psi_w)},$$

with

$$\delta\psi(u) = \frac{12}{\sqrt{30}\pi} \frac{92}{45} u^5 + O(u^{10})$$

the largest growing phase drift.  $A_w$  and  $\psi_w$  are small modulations in the amplitude and phase oscillating as a function of frequency. Since for all observed frequencies  $f_{\text{gw}}$  and chirp masses  $\mathcal{M}$  used in this thesis,  $u = (\pi f_{\text{gw}} \mathcal{M})^{1/3} \ll 1$ , it is clear that this correction term is negligible.

Furthermore, Droz. *et al.* have numerical Fourier transforms (also known as *Fast Fourier Transforms*) to numerically approximate the waveform without a SPA, and compared this to the analytical waveform with the SPA. They defined a quantity called *overlap*, which is defined in equation (4.1) of [24] to be

$$\mathcal{O} = \frac{(\tilde{h}_{\text{fft}}|\tilde{h}_{\text{spa}})}{\sqrt{(\tilde{h}_{\text{fft}}|\tilde{h}_{\text{fft}})(\tilde{h}_{\text{spa}}|\tilde{h}_{\text{spa}})}}, \quad (3.10)$$

where  $h_{\text{fft}}$  is the numerical waveform,  $h_{\text{spa}}$  is the analytical waveform using the SPA, and we use the notation

$$(a|b) = 2 \int_{F_{\min}}^{F_{\max}} \frac{a^*(f)b(f) + a(f)b^*(f)}{S_n(f)} df$$

with  $S_n$  the spectral density of the noise of the used detector. The overlap for several different waveforms are given in table 3.3.1.

$\mathcal{M}(M_{\odot})$	1.00	1.25	1.50	1.75	2.00	2.25	2.50	2.75	3.00	10.00
$\mathcal{O}$	0.9999	0.9998	0.9997	0.9997	0.9996	0.9994	0.9994	0.9994	0.9994	0.9972

Table 1: Data adapted from table 1 of [24], with  $\mathcal{M}$  defined in equation 4.5 and in solar masses, and  $\mathcal{O}$  as defined in equation 3.10.

As can be seen, the overlap is very close to unity, even for high masses. Due to this high accuracy in both the analytical and numerical tests, we conclude that the SPA is a very accurate approximation and we will thus use it in this thesis.

## 4 Post Einsteinian theories of Gravity and their Waveforms

In this section, we will take a look at how the different polarisations are detected by an interferometer. First, we introduce different theories of gravity and their polarisation modes in section 4.1. After this, we treat how the orientation of the detector changes the observed signal in section 4.2. We will then give the full equations for each different polarisation in section 4.3.

### 4.1 Non-GR theories and polarisations

Until now, we exclusively treated General Relativity. However, this is not the only theory of gravity, albeit the most accepted. In this thesis, 3 alternative theories of gravity are also considered: Brans-Dicke[6], Rosen [8][9] and Lightman-Lee[7]. These theories have been chosen as they have (historically) been seen as viable alternatives for GR, and are all metric theories of gravity. A theory of gravity is a metric theory when it satisfies two conditions[25]:

- The theory contains a metric containing proper length  $s$  and proper time  $\tau$  via the equation  $ds^2 = g_{\mu\nu} dx^\nu dx^\mu$ ,



- The stress-energy tensor  $T$  for all matter and fields satisfies  $\nabla \cdot T = 0$  when acted upon by gravity.

Since they are all metric theories, the tidal force equation 2.7 holds true, and their gravitational waves also contain polarisations. However, were we found that GR only contains  $h_+$  and  $h_\times$  in section 2.3.4, these theories also contain extra terms. Below in table 4.1, a overview has been given for all the polarisation modes which are present in the used theories. Apart from the plus and cross polarisation modes  $h_+$  and  $h_\times$ , the  $x$  and  $y$  vector modes  $h_{Xvec}$  and  $h_{Yvec}$ , the breathing mode  $h_B$ , and the longitudinal mode  $h_L$ .

Theory of gravity	$h_+$	$h_\times$	$h_B$	$h_L$	$h_{Xvec}$	$h_{Yvec}$
GR	✓	✓				
Brans-Dicke <sup>1</sup>	✓	✓	✓			
Rosen	✓	✓	✓	✓	✓	✓
Lightman-Lee	✓	✓	✓	✓	✓	✓

Table 2: Data adapted from [26] and [23]. <sup>1</sup>In Brans-Dicke theory, if the graviton is massive, there is also a longitudinal mode which is correlated to the breathing mode. In this thesis, we consider the hypothetical graviton to be massless.

These polarisation modes enter a matrix  $A_{\alpha\beta}$  the same way as equation 2.14 in GR, which for all the theories takes the form

$$h_{\alpha\beta} = \begin{pmatrix} h_B + h_+ & h_\times & h_{Xvec} \\ h_\times & h_B - h_+ & h_{Yvec} \\ h_{Xvec} & h_{Yvec} & h_L \end{pmatrix}, \quad (4.1)$$

where modes that are not present are set to be equal to zero. From this equations we can derive the equations of motion for every theory of gravity in a similar method as seen in section 2.3.4. The effects of these polarisations on a ring of test particles are seen in figure 3.

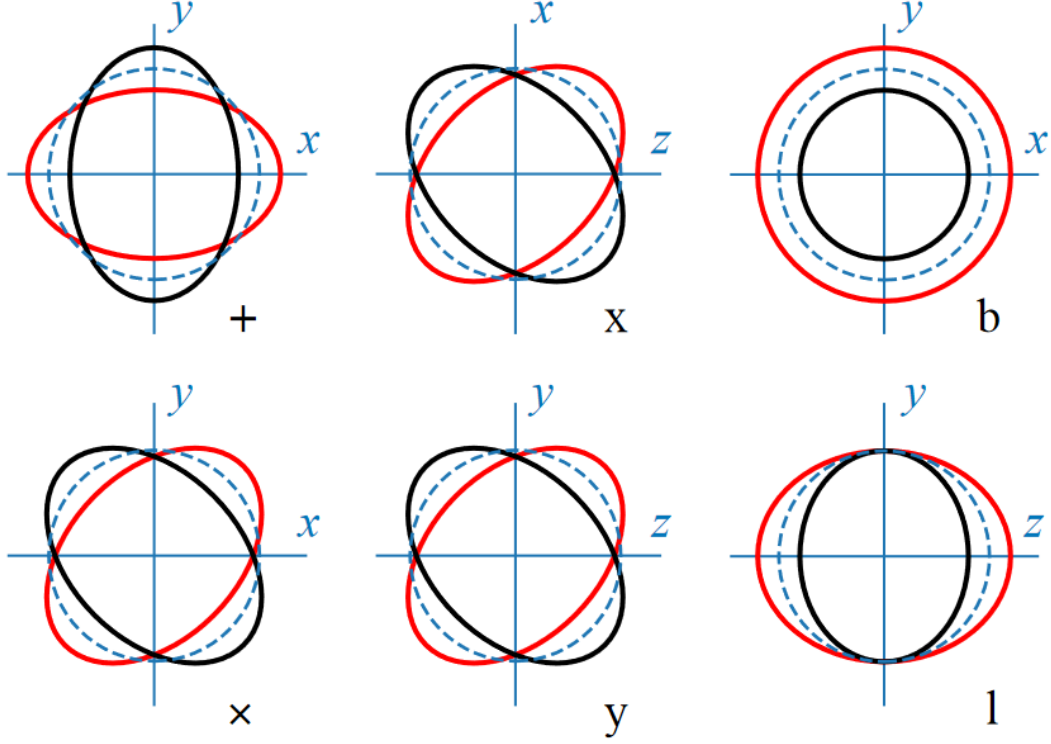


Figure 3: The effects of the different polarisation modes on a ring of test particles. The gravitational wave in this example propagates in the direction of the z-axis. The dotted line resembles the ring of particles under no metric perturbations, and the red and black lines are the configurations of the particles which it oscillates between when the polarisation is present. Adapted from figure 1 of [10].

## 4.2 Orientation of the detectors and measured signal

In this section we will give full equations for all polarisation modes for every treated theory of gravity. The total waveform as measured by the interferometer, also called the *strain*, is given by the sum of all the polarisations times a factor which determines the sensitivity of the interferometer for that particular polarisation. In formula-form, the strain  $S(t)$  is given by

$$S(t) = F_+ A_+ + F_\times A_\times + F_B A_B + F_L A_L + F_{Xvec} A_{Xvec} + F_{Yvec} A_{Yvec}, \quad (4.2)$$

where  $h_i$  is the polarisation mode as given in equation 4.1, and  $F_i$  is the *angular pattern function* of this polarisation, which we will now derive.

As evident from figure 3, the orientation of an interferometer with respect to the incoming wave is of direct influence on the measured polarisation modes: if it points in a direction perpendicular to the plane of perturbation of a polarisation, it won't measure it. The *angular pattern functions* tell us what fraction of each polarisation is measured, based on the orientation of the interferometer. First, we construct a matrix  $h'_{\alpha\beta}$ , which is the matrix  $h_{\alpha\beta}$  from equation 4.1 containing all the polarisation modes, rotated using the standard spherical coordinates as given in

the rotation matrix  $R$ . Then,  $h'_{\alpha\beta}$  is given by [21]

$$h'_{\alpha\beta} = (R h_{\alpha\beta} R^T)_{\alpha\beta}, \quad (4.3)$$

with the rotation matrix  $R$  given by

$$R = \begin{pmatrix} \cos \phi & \sin \phi & 0 \\ \sin \phi & \cos \phi & 0 \\ 0 & 0 & 1 \end{pmatrix} \begin{pmatrix} 1 & 0 & 0 \\ 0 & \cos \theta & -\sin \theta \\ 0 & \sin \theta & \cos \theta \end{pmatrix} \begin{pmatrix} \cos \psi & \sin \psi & 0 \\ -\sin \psi & \cos \psi & 0 \\ 0 & 0 & 1 \end{pmatrix},$$

and  $R^T$  being the transposed matrix of  $R$ . Here, the rotational parameters  $\phi, \theta$  and  $\psi$  are as defined in figure 4.

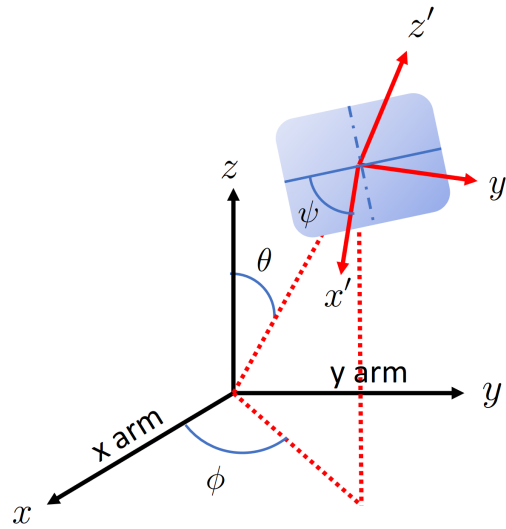


Figure 4: The rotational parameters  $\phi$ , and  $\psi$  which define the the orientation of one set of axis to another. Adapted from [21].

The full strain measured by an interferometer is given by [23]

$$S(t) = \frac{1}{2} (\hat{e}_1^i \hat{e}_1^j - \hat{e}_2^i \hat{e}_2^j) h'_{ij},$$

where  $\hat{e}_1$  and  $\hat{e}_2$  are basis vectors in the directions of the arms of the interferometer. If we take them to be along the  $x$  and  $y$ -axis, so  $\hat{e}_1 = (1, 0, 0)$  and  $\hat{e}_2 = (0, 1, 0)$ , and substitute equation 4.3, we arrive at an equation in the form of equation 4.2, with the angular pattern functions  $F_i(\theta, \phi, \psi)$  given by:

$$\begin{aligned}
F_+ &= \frac{1}{2}(1 + \cos^2 \theta) \cos 2\phi \cos 2\psi - \cos \theta \sin 2\theta \sin 2\psi \\
F_\times &= \frac{1}{2}(1 + \cos^2 \theta) \cos 2\phi \sin 2\psi + \cos \theta \sin 2\theta \cos 2\psi \\
F_B &= -\frac{1}{2} \sin^2 \theta \cos 2\phi \\
F_L &= \frac{1}{2} \sin^2 \theta \cos 2\phi \\
F_{Xvec} &= -\sin \theta (\cos \theta \cos 2\phi \cos \psi - \sin 2\phi \sin \psi) \\
F_{Yvec} &= -\sin \theta (\cos \theta \cos 2\phi \sin \psi + \sin 2\phi \cos \psi).
\end{aligned}$$

### 4.3 Waveforms

#### 4.3.1 New parameters

In the non-GR theories we discuss in this thesis, a concept of *sensitivity* is introduced. It is defined as the sensitivity of an object to changes in the gravitational constant  $G$  [27]: in GR and Newtonian gravity, this is evidently a constant, but in Brans-Dicke, Rosen and Lightman-Lee theories of gravity it is not. It is formally defined as

$$s = - \left( \frac{\partial \ln M_i}{\partial \ln G} \right)_N, \quad (4.4)$$

with  $M_i$  the inertial mass of the object and  $N$  the baryon number. It has been shown that for normal stars, this sensitivity would be  $s_{n*} \sim 10^{-6}$ , for white dwarfs the sensitivity would be  $s_{WD} \sim 10^{-3}$ , neutron stars have a sensitivity between  $s_N \sim 0.1$  and  $s_N \sim 0.4$ , and black holes have a theoretical limit of  $s_{BH} = 0.5$  [27][28].

As will be seen in the following parts of this section, the non-GR theories mainly depend on the difference in scalar charge of the two objects. Therefore, it is best to chose a system where this difference is as large as possible.

#### 4.3.2 GR

From equations (30)-(34) of [23], we can derive the full expressions for every polarisation mode present in GR:  $h_+$  and  $h_\times$ . We give the Fourier transforms of the polarisations using the SPA as discussed in previous sections. The response functions are:

$$\begin{aligned}
\tilde{h}_+^{GR} &= - \frac{\sqrt{\frac{5\pi}{6}} (\mathcal{M}\pi)^{1/6} e^{-i\Psi_{GR}^{(2)}} (1 + \cos^2 \iota)}{4Du_{(2)}^{7/2}}, \\
\tilde{h}_\times^{GR} &= - \frac{\sqrt{\frac{5\pi}{6}} (\mathcal{M}\pi)^{1/6} i e^{-i\Psi_{GR}^{(2)}} \cos \iota}{2Du_{(2)}^{7/2}}.
\end{aligned}$$

Here,  $D$  is the distance from the observer to the source,  $\mathcal{M}$  is the *chirp mass*, which is given by

$$\mathcal{M} = \frac{(m_1 m_2)^{3/5}}{(m_1 + m_2)^{1/5}}, \quad (4.5)$$

$u_{(2)}$  is a parameter given by

$$u_{(l)} = \left( \frac{2\pi \mathcal{M} f}{l} \right)^{1/3} \quad (4.6)$$

where  $f$  is the frequency of the wave, and  $\Psi_{GR}^{(2)}$  is the GR phase to the 0PN order given by:

$$\Psi_{GR}^{(l)} = -2\pi f t_c + l\phi_c/2 + \frac{\pi}{4} - \frac{3l}{256u_{(l)}^5}. \quad (4.7)$$

### 4.3.3 Brans-Dicke

From equations (48)-(56) of [23], we can derive the full expressions for every polarisation mode present in the Brans-Dicke theory of gravity:  $h_+$ ,  $h_\times$  and  $h_B$ . We give the Fourier transforms of the polarisations using the SPA as discussed in previous sections. A parameter unique to Brans-Dicke is the *Brans-Dicke coupling constant*  $\omega_{BD}$ , which determines the deviation from GR. In the limit that  $\omega_{BD} \rightarrow \infty$ , the expressions for GR are obtained. From observations made by the Cassini spacecraft, the minimum value of this constant is set to be  $\omega_{BD} > 40000$  [29]. A different constant  $k_{BD} = \frac{1}{2} + \frac{2}{3}(s_1 + s_2 - 2s_1s_2)$  only depends on the scalar charges as defined in ?? . The response functions are:

$$\begin{aligned} \tilde{h}_+^{BD} &= \frac{\sqrt{\frac{5\pi}{6}} e^{-i\Psi_{BD}^{(2)}} \mathcal{M}^2 B_{BD} (k_{BD}\xi - 1) (1 + \cos^2 \iota)}{384u_{(2)}^{11/2} D} \\ \tilde{h}_\times^{BD} &= \frac{\sqrt{\frac{5\pi}{6}} e^{-i\Psi_{BD}^{(2)}} i \mathcal{M}^2 B_{BD} (k_{BD}\xi - 1) \cos \iota}{192u_{(2)}^{11/2} D} \\ \tilde{h}_B^{BD} &= -\frac{\sqrt{\frac{5\pi}{6}} e^{-i(\Psi_{BD}^{(1)} + \Psi_{BD}^{(2)})} \mathcal{M}^2 \xi \sin(\iota) (96e^{i\Psi_{BD}^{(2)}} u_{(2)} S \eta^{1/5} - e^{i\Psi_{BD}^{(1)}} B_{BD} \Gamma \sin \iota)}{768u_{(2)}^{11/2} D} \end{aligned}$$

where  $\xi = (2 + \omega_{BD})^{-1}$ ,  $\Gamma = 1 - 2(m_1s_2 + m_2s_1)/m_{tot}$ ,  $S = s_1 - s_2$ ,  $\mathcal{M}$  is given in equation 4.5,  $\iota$  is the angle between the observer and the plane of coalescence, and the *symmetric mass ratio*  $\eta$  given by

$$\eta = \frac{m_1 m_2}{(m_1 + m_2)^2}, \quad (4.8)$$

and we defined for easy handling of the equations that

$$\begin{aligned} A_{BD} &= 24 + 12k_{BD}\xi - \Gamma^2\xi \\ B_{BD} &= 4A_{BD}u_2^2 - 5S^2\eta^{2/5}\xi. \end{aligned}$$

The Brans-Dicke phase  $\Psi_{BD}^{(l)}$  is given by

$$\Psi_{BD}^{(l)} = \Psi_{GR}^{(l)} + \frac{5l}{7168} \xi S^2 \eta^{2/5} u_{(l)}^{-7},$$

with  $\Psi_{GR}^{(l)}$  the GR phase as defined in equation 4.7.

#### 4.3.4 Rosen

From equations (64)-(72) of [23], we can derive the full expressions for every polarisation mode present in the Rosen theory of gravity:  $h_+$ ,  $h_\times$ ,  $h_B$ ,  $h_L$ ,  $h_{Xvec}$  and  $h_{Yvec}$ . We give the Fourier transforms of the polarisations using the SPA as discussed in previous sections. The Rosen coupling constant is given by  $k_R = 1 - 4s_1s_2/3$ , with  $s_i$  the sensitivity of the  $i$ -th object as defined in section ?? . We deviate from the definition of the original paper, since there was most likely an error in the definition of the constant  $\mathcal{G}$  [30]. We follow *Wong et al.* in their definition of  $\mathcal{G} = s_1 - s_2$ . The full expressions for each polarisation mode reads:

$$\begin{aligned}\tilde{h}_+^R &= \frac{\sqrt{\frac{5\pi}{21}} e^{-i\Psi_R^{(2)}} \mathcal{M}^2 (1 + \cos^2(\iota))}{4Dk_R^{3/4} u_{(2)}^{7/2}} \\ \tilde{h}_\times^R &= \frac{\sqrt{\frac{5\pi}{21}} e^{-i\Psi_R^{(2)}} \mathcal{M}^2 \cos(\iota)}{4Dk_R^{3/4} u_{(2)}^{7/2}} \\ \tilde{h}_B^R &= -\frac{\sqrt{\frac{5}{21}} \pi^{1/3} i e^{-i(\Psi_R^{(1)} + \Psi_R^{(2)})} \mathcal{M}^2 \sin(\iota) (A_R + B_R)}{12Dk_R^{3/4} u_{(2)}^2} \\ \tilde{h}_L^R &= -\frac{\sqrt{\frac{5}{21}} \pi^{1/3} i e^{-i(\Psi_R^{(1)} + \Psi_R^{(2)})} \mathcal{M}^2 \sin(\iota) B_R}{6Dk_R^{3/4} u_{(2)}^2} \\ \tilde{h}_{se}^R &= -\frac{\sqrt{\frac{5}{21}} \pi^{1/3} i e^{-i(\Psi_R^{(1)} + \Psi_R^{(2)})} \mathcal{M}^2 \cos(\iota) B_R}{6Dk_R^{3/4} u_{(2)}^2} \\ \tilde{h}_{sn}^R &= \frac{\sqrt{\frac{5}{21}} \pi^{1/3} e^{-i(\Psi_R^{(1)} + \Psi_R^{(2)})} \mathcal{M}^2 B_R}{6Dk_R^{3/4} u_{(2)}^2},\end{aligned}$$

where  $\mathcal{M}$  is given in equation 4.5,  $\iota$  is the angle between the observer and the plane of coalescence, and  $u_{(l)}$  in equation 4.6. We have defined the following for easy handling of the equations

$$\begin{aligned}A_R &= 2e^{i\Psi_R^{(2)}} \mathcal{G} k_R^{1/6} \eta^{1/5} \\ B_R &= A_R + 3e^{i\Psi_R^{(1)}} u_{(2)} \sin(\iota),\end{aligned}$$

where  $\eta$  is given in equation 4.8, and the phase of the gravitational wave is given by

$$\Psi_R^{(l)} = \pi/4 + l\Phi_c - 2\pi f t_c + \frac{3l}{224u_{(l)}^5} k_R^{-5/6} + \frac{25l}{8232} \frac{\mathcal{G}^2 \eta^{2/5}}{u_{(l)}^7} k_R^{-2/3}$$

#### 4.3.5 Lightman-Lee

From equations (80)-(88) of [23], we can derive the full expressions for every polarisation mode present in the Lightman-Lee theory of gravity:  $h_+$ ,  $h_\times$ ,  $h_B$ ,  $h_L$ ,  $h_{Xvec}$  and  $h_{Yvec}$ . We give the Fourier transforms of the polarisations using the SPA as discussed in previous sections. We again use the modified expression of  $\mathcal{G} = s_1 - s_2$ . The full expression for each polarisation

mode reads

$$\begin{aligned}
\tilde{h}_{\times}^{LL} &= \frac{\sqrt{\frac{5\pi}{21}} e^{-i\Psi_{LL}^{(2)}} \mathcal{M}^2 \cos(\iota)}{2DB_{LL}^{7/2}} \\
\tilde{h}_{+}^{LL} &= -\frac{\sqrt{\frac{5\pi}{21}} i e^{-i\Psi_{LL}^{(2)}} \mathcal{M}^2 (3 + \cos(2\iota))}{4DB_{LL}^{7/2}} \\
\tilde{h}_B^{LL} &= \frac{\sqrt{\frac{5\pi}{21}} i e^{-i(\Psi_{LL}^{(1)} + \Psi_{LL}^{(2)})} \mathcal{M}^2 \sin(\iota) (-5A_{LL} + 6B_{LL})}{24DB_{LL}^{9/2}} \\
\tilde{h}_L^{LL} &= -\frac{\sqrt{\frac{5\pi}{21}} i e^{-i(\Psi_{LL}^{(1)} + \Psi_{LL}^{(2)})} \mathcal{M}^2 \sin(\iota) (A_{LL} + B_{LL})}{6DB_{LL}^{9/2}} \\
\tilde{h}_{se}^{LL} &= \frac{\sqrt{\frac{5\pi}{21}} i e^{-i(\Psi_{LL}^{(1)} + \Psi_{LL}^{(2)})} \mathcal{M}^2 \cos(\iota) (A_{LL} - B_{LL})}{6DB_{LL}^{9/2}} \\
\tilde{h}_{sn}^{LL} &= \frac{\sqrt{\frac{5\pi}{21}} \mathcal{M}^2 (-5e^{-i\Psi_{LL}^{(1)}} \mathcal{G} \eta^{1/5} + 3e^{-i\Psi_{LL}^{(2)}} u_2 \sin(\iota))}{6DB_{LL}^{9/2}},
\end{aligned}$$

where  $\mathcal{M}$  is given in equation 4.5,  $\iota$  is the angle between the observer and the plane of coalescence,  $u_{(l)}$  in equation 4.6 and  $\eta$  in equation 4.8, and we have defined

$$\begin{aligned}
A_{LL} &= 5e^{i\Psi_{LL}^{(2)}} \mathcal{G} \eta^{1/5} \\
B_{LL} &= 3e^{i\Psi_{LL}^{(1)}} u_2 \sin(\iota)
\end{aligned}$$

and the phase of the gravitational wave is given by

$$\Psi_{LL}^{(l)} = \pi/4 + l\Phi_c - 2\pi f t_c + \frac{3l}{224u_{(l)}^5} - \frac{625l}{16464} \frac{\mathcal{G}^2 \eta^{2/5}}{u_{(l)}^7}.$$

## 5 Lensing of Gravitational Waves

In this section, we look at how a gravitational lens can produce multiple images of the same gravitational wave. In section 5.1, we will take a look at the basic principles and equations of gravitational lensing. After this, we will see in section 5.2 in what way the gravitational wave changes after it is lensed. Finally, we will look at some research to find how often a lensed gravitational wave is expected to be detected in section 5.3.

### 5.1 Basic Principles of Gravitational Lensing

In this section, we will follow chapter 1 and 2 of [11].

During this section and the remainder of this thesis, we are talking about gravitational lensing as described in the theory of General relativity. However, for alternative theories of gravity, gravitational lensing might also work differently [31] [32]. Since there has been nearly no work

done in this field, we assume lensing is not significantly different in other theories of gravity, and thus follow the GR equations for every theory.

As we have seen in section 1, space is deformed around gravitational fields. When we introduce a gravitational potential  $\Phi$  to a flat Minkowski space, the metric takes the form as defined in equation (1) of [33]

$$g_{\mu\nu} = \begin{pmatrix} -(1+2\Phi) & 0 & 0 & 0 \\ 0 & 1-2\Phi & 0 & 0 \\ 0 & 0 & 1-2\Phi & 0 \\ 0 & 0 & 0 & 1-2\Phi \end{pmatrix}, \quad (5.1)$$

where  $\Phi \ll 1$ . An object which creates such a gravitational potential is called a *weak lens*, which we will consider here. Light that comes near such an object travels through this curved space-time, and thus follows a curved path, much like an optical lens. These lenses can be anything that generates a strong gravitational field: stars, black holes or even entire galaxies. Note that when the gravitational wave passes too close to these objects (and thus  $\Phi$  grows too large), they behave as *strong lenses*, and the equations shown in this section do not necessarily hold true. The principles of lensing stay the same, and can be applied to both weak and strong lenses. For the remainder of this thesis, we make the assumption that our lenses are point-lenses: the lensing object is a point mass.

From the equation above, it follows that the speed of light on a path through this curvature is reduced. If we insert equation 5.1 into the equation for the proper distance between two points, equation 2.2, we obtain that for  $ds^2 = 0$  (the light-like path gravitational waves follow in GR) the speed of light is equal to

$$c' = \sqrt{\frac{1+2\Phi}{1-2\Phi}} \approx 1 + 2\Phi.$$

Note that  $\Phi$  is negative, and thus the speed of light (and gravitational waves) is smaller than in a pure vacuum. Due to this, a gravitational wave has a longer travel time through the distorted space-time, an effect called the *Shapiro time delay*[34]. This delay  $\Delta t$  is given by

$$\Delta t_S = \int \frac{dl}{c'} - \int dl = -2 \int \Phi dl. \quad (5.2)$$

It is thus clear that two gravitational waves that are created at the same time and travel the same distance to our detectors do not arrive at the same time if one of them enters a gravitational field on the way, but the other does not.



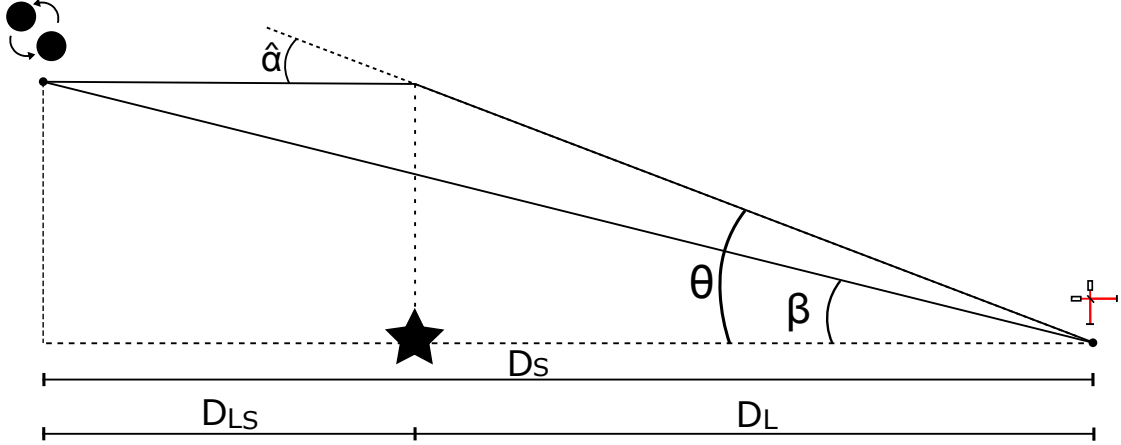


Figure 5: A schematic view of a possible lensed event.  $D_S$  is the distance from the observer (the interferometer on the right hand side) to the plane of the event (the two bodies in inspiral on the left hand side),  $D_{LS}$  is the distance from the lensing plane (the star) to the plane of the event, and  $D_L$  is the distance from the observer to the lensing plane. Note that  $D_S \neq D_{LS} + D_L$ .  $\hat{\alpha}$  is the angle of curvature of the path as defined in equation 5.4,  $\beta$  is the angle between the lens, the observer and the event, and  $\theta$  is the angle between the lens, the observer and the lensed gravitational wave.

The gravitational wave does not only slow down in the distorted space-time however, its path is also curved. From figure 5, a geometric construction can be used when the angles  $\vec{\theta}$ ,  $\vec{\beta}$  and  $\hat{\alpha}$  are small, so they are related via the so called *lens equation*:

$$\vec{\theta} D_S = \vec{\beta} D_S + \hat{\alpha} D_{LS} \quad (5.3)$$

It can be shown after some algebra that the path curves by an angle  $\hat{\alpha}$ ,

$$\hat{\alpha} = 2 \int_{e_A}^{e_B} \vec{\nabla}_{\perp} \Phi d\vec{e}, \quad (5.4)$$

where  $\vec{\nabla}_{\perp}$  are the vectorial derivatives perpendicular to the direction of motion, and  $\vec{e}$  is the unit vector tangent to the direction of motion. For a point mass, this equation takes the very simple form

$$\hat{\alpha} = 4 \frac{M}{b},$$

where  $M$  is the mass of the point mass, and  $b$  the shortest distance between the lensing object and the path of the wave if it would not have been lensed.

Using equation 5.2 and 5.4, we can determine a total difference in travelling time  $\Delta t$  between a straight path and a lensed path between the source and an observer. We can take this difference in time to be

$$\Delta t = \Delta t_S + \Delta t_{\text{path}},$$

where  $\Delta t_{\text{path}}$  is the difference in travel time due to the difference in path length. After some very involved calculus (see also section 3.4.2 from [12]), the full equation for the time delay for point-lenses can be shown to be equal to equation (3.110) from [12]:

$$\Delta t = \frac{D_L D_S}{2 D_{LS}} (\vec{\beta} - \vec{\theta})^2 - 4M \ln |\vec{\theta}|. \quad (5.5)$$

Note that in the case that  $|\vec{\beta}|, |\vec{\theta}|, |\hat{\alpha}| \ll 1$  [11], we can use equation 5.3 to simplify the above to

$$\Delta t = \frac{D_L D_{LS}}{2D_S} \hat{\alpha}^2 - 4M \ln |\vec{\theta}|.$$

examine a very interesting scenario. A gravitational wave is created by two super heavy objects in inspiral, such as black holes or neutron stars, and is sent towards the Earth. It is possible that this gravitational wave reaches our detectors twice or more when one so called *image* of the gravitational wave reaches us via a nearly straight path, and one reaches us via a more curved trajectory involving a lens.. It is clear that there is a time delay between the arrival of the two images due to the difference in path length, and that we can thus detect the same wave twice.

This is of great interest, since this allows us to probe the polarisations of the gravitational waves more deeply. If the lensing occurred very far away from the Earth, we can state that the two gravitational waves come from the same direction in the sky: the deflection angle for strongly lensed waves is in the order of magnitude of  $|\hat{\alpha}| \approx \sqrt{M/10^{21} M_\odot}$  arcseconds, with  $M$  the mass of the lens and  $M_\odot$  a solar mass, or  $2 \times 10^{30}$  kg [32]. It follows that the difference in direction of the two images can be put to zero to good approximation. The first image is detected by our interferometers, which arms point in a certain direction and thus measure the metric perturbations in those directions. When the second image of the wave arrives after some time, the Earth has rotated around its axis by a certain amount. Due to this, the same detectors now point in a different direction when viewed from the sky. These detectors now measure the metric perturbations of the same wave but now from a different angle. We can thus combine these two sets of measurement to very accurately determine in what directions the wave perturbed the metric, and thus what polarisations are present. This result could be used as a test for general relativity: if more modes are present than just the plus and cross polarisations (see also table 4.1), this means a correction of the theory is necessary.

## 5.2 Effect on Gravitational Waveform

Gravitational lenses do not only change the velocity and direction of a gravitational wave, but also change the wave itself.

The main effect is magnification: when a gravitational wave passes a lens, two images arrive at the observer with a difference in amplitude. Their amplitudes are governed by equation (18) from [35]:

$$F(f) = \sqrt{|\mu_+|} + i\sqrt{|\mu_-|} e^{2\pi i f \Delta t}, \quad (5.6)$$

where  $f$  is the frequency of the wave,  $\Delta t$  is the time delay between images as defined in equation 5.5, and

$$\mu_{\pm} = \frac{1}{2} \pm \frac{y^2 + 2}{2y\sqrt{y^2 + 4}}$$

is the so called *magnification factor* of each image.  $y$  is a parameter expressing the location of the lens, with  $y = \beta (4MD_{LS}/(D_L D_S))^{-1/2}$  [11]. It follows from this that the amplitude of the lensed wave is always larger than the unlensed wave. A ratio between the two, called the *magnification ratio* is simply given by

$$\mu = \left( \left| \frac{\mu_-}{\mu_+} \right| \right)^{1/2} = \frac{y - \sqrt{y^2 + 4}}{y + \sqrt{y^2 + 4}}. \quad (5.7)$$

This  $\mu$  is what we will be measuring during the thesis, not the individual magnification factors  $\mu_+$  and  $\mu_-$ , simply because we cannot measure them individually. Because all waves go as one over distance, as seen in section 4.3, the amplitude of the wave is directly correlated with the distance. Because of this, we can't determine the "real" distance between us and the origin of the gravitational wave, since both waves have a modified amplitude and thus different apparent distance travelled. However, the first image to arrive is the least magnified the two, since its path was the most direct and thus the least lensed. Because of this, we will be taking determining the apparent distance as conveyed by the first image during this thesis. Do keep in mind that while this might me a good approximation for the real distance depending on the value of the magnification ratio, this is not the real distance between us and the event.

The lens also has an effect on the polarisation tensor of the gravitational wave, either changing the contents of the polarisation vector [35] or having the different polarisations arrive at different times at the detector [32]. However, in both cases, it is shown that this effect is so small that it is immeasurable, and we thus take it that the lens only scales the amplitude of the wave.

### 5.3 Lensing rates

It is of course of interest how often we expect to detect a lensed gravitational wave for the relevance of the research as presented here. For the purpose of this thesis, we are actually talking about a *double lensed event* [36]: a gravitational wave which is detected twice by the detectors. For the results as presented below, we expect an image to be detected when it has a  $\text{SNR} > 8$ , with SNR as defined in equation 6.5.

It is possible that there are additional images of the wave, but that these are too weak to be detected. It is also possible to have waves which are lensed thrice or more times, but these fall beyond the scope of this paper. It should however be very easy to expand the procedures as developed for this thesis for these cases. A recent statistical model study by Wierda *et al.* has looked into this and presented the results as seen in table 3.

Lensed Events	L/H/V/K	L/H/V/K (A+)
Double	$0.92^{+0.46}_{-0.31} \text{ yr}^{-1}$	$2.5^{+1.2}_{-0.8} \text{ yr}^{-1}$
Triple	$0.23^{+0.12}_{-0.08} \text{ yr}^{-1}$	$0.55^{+0.28}_{-0.19} \text{ yr}^{-1}$
Quadruple	$0.12^{+0.06}_{-0.04} \text{ yr}^{-1}$	$0.30^{+0.15}_{-0.10} \text{ yr}^{-1}$
Total	$1.3^{+0.6}_{-0.4} \text{ yr}^{-1}$	$3.3^{+1.7}_{-1.1} \text{ yr}^{-1}$
Unlensed	$1.9 \times 10^3 \text{ yr}^{-1}$	$5.8 \times 10^3 \text{ yr}^{-1}$

Table 3: The rate at which lensed gravitational waves are detected for a detector network consisting of 4 detectors (LIGO Livingston [L], LIGO Hanford [H], Virgo [V] and KAGRA [K]). Data adapted from table 1 of [36]. The uncertainties are at a 90% confidence level. The [V] and [K] detectors are always at their design sensitivity, [L] and [H] are at their design sensitivity in the first row, and at their sensitivities after the A+ upgrade in the second.

The A+ sensitivities of the LIGO detectors are expected to be operational in 2024[37].

## 6 Model selection and Parameter Estimation

In this section, we will take a look at how the data from a gravitational wave detector is processed. In section 6.1, we take a look at the noise in a detector: what does it look like and what are its origins? We then continue with section 6.2, where we treat Bayes' theorem. After this, in section 6.3, we treat how to use calculations to extract the parameters of the binary system which caused the gravitational wave from the data.

### 6.1 Characteristics of the noise

For this subsection, we will follow sections 2.1 and 2.2 of [15], where a more thorough treatment of this subject can be found.

Most of what a GW detector measures is noise, with the occasional signal buried within it. To be able to extract the weak signal (often in the order of  $10^{-21}$ ), we need a good understanding of what the noise looks like. First we will treat what causes the noise, then some mathematical characterisations of this noise.

#### 6.1.1 Cause of noise

This subsubsection follows section V of [38]. The interferometers used (very simply said) use the displacement of the mirrors at the end of the arms to measure the change of the length of the arms. The problem is that not only the distortions of space-time of gravitational waves change the positions of the mirrors: unwanted movements of the mirrors is created by *displacement noise*. Furthermore, some effects cause differences in the phase of the lasers, which also leads to different measurements since the difference of the phase of the two beams is used through interference to determine the difference in length of the arms of the detector. This type of noise is called *phase noise*.

The displacement noise is given by:

- **Mirror thermal noise.** These are mainly in the mirror coating of the mirror, not the bulk material. These coatings typically have very internal friction quality, and thus are very prone to Brownian effects. Small thermodynamic fluctuations of the temperature of the coating also produces noise, but create small differences in the refraction index of the mirror too.
- **Suspension thermal noise.** The mirrors of the detectors are kept into place by a suspension system to isolate it from external vibrations, and to allow it to move separately from the detector when a gravitational wave passes. This is mainly done by hanging the mirror by a thin fibre, so the mirror acts as a pendulum. This makes it that there is nearly no thermal noise through the suspension, but it is not fully eliminated.
- **Tidal forces.** The tidal forces of the Sun and the Moon create the largest differences in length of the detector: for a 4km detector arm this effect is around 100-200  $\mu\text{m}$ . This is mostly compensated by actuators in the detector arms itself.
- **Seismic vibrations.** While it is easy to see that a large-scale earthquake would create a gigantic amount of noise (and damage the detector in the process), *secondary microseism* are the second largest cause of length change of the arms of a detector. These very small earthquakes change the length of the arms by several  $\mu\text{m}$ , and are compensated by sensors within the detector arms itself.

- **Newtonian gravity noise.** Due to changes in density of for example the atmosphere, the local gravitational force on the mirrors changes, causing small movements of the mirrors.
- **Electromagnetic coupling.** The cosmic background rays of (mostly) muons ionize the electrons of the mirrors, adding kinetic energy in the process. The changes in the background magnetic fields also influence magnets used in the interferometer.

The phase noise is given by:

- **Quantum effects.** A series of different quantum effects, such as the difference in arrival time of the separate photons that make up the laser, create a noise in the phase.
- **Scattering from residual gas.** Since a perfect vacuum is not attainable, the interferometers are filled with gasses of particles of very low density which cause as little scattering as possible with the lasers. Slight differences in the density of these gasses cause slight differences in the optical phase of the laser.
- **Backscatter.** Due to slight imperfections in the shape of the mirrors, the light can reflect diffusely, causing noise in the phase.

### 6.1.2 Power spectral density

The noise is a so called *random wide-sense stationary process*. If we take that the noise output is given by a random function  $x(t)$ , this means that the statistical properties of  $x(t)$  are independent of time. The mean value of  $E[x(t)]$  is a constant for every time  $t$  (with  $E[\cdot]$  the ensemble average), and the autocorrelation function  $E[x(t)x(t')]$  only depends on the time shift  $\Delta t = t - t'$ . A very helpful way of characterising the noise is through the so called *power spectral density* of the noise. This function shows the correlation of the noise with itself over frequency. It can be shown (equation (2.1) of [15]) that via a Fourier transform, the autocorrelation function of the noise is given by

$$E[\tilde{x}(f)\tilde{x}^*(f')] = \mathcal{N}(f)\delta(f - f'), \quad (6.1)$$

where  $\delta$  is the Dirac delta function, and  $\mathcal{N}$  is the power spectral density. The noise is thus a collection of random events  $\tilde{x}(f)$  with variance  $\mathcal{N}$ . If the power spectral density is a constant, there is no dependence on frequencies, and we speak of *white noise*, otherwise we call the noise *coloured noise*.

### 6.1.3 Gaussian noise

A linear combination of a large number of independent random processes can be approximated by a Gaussian random process. Gaussian noise is thus the main part of the noise in the detector. During normal simulations, a set of Gaussian noise is added to simulate all the noise in the interferometer. During this bachelor project, we sadly could not do this due to time constraints: the inclusion of noise creates a very heavy computational workload. For completeness sake, we have included the very basics of this noise.

We can write this combination of random events as the vector  $\vec{x}$ , with the contents  $x_i = x(t_i)$  and  $t_i = (i - 1)T/N$ , where  $T$  is the total time and  $N$  the step size of the time. The probability distribution function (pdf) of this random process is given by the  $N$ -th dimensional Gaussian distribution function

$$\text{pdf}(\vec{x}) = \frac{1}{\sqrt{(2\pi)^N \det(\mathbf{C})}} \exp\left[-\frac{1}{2}(\vec{x} - \vec{\mu}|\vec{x} - \vec{\mu})\right], \quad (6.2)$$

with  $\vec{\mu}$  a vector containing the average  $\mu_i$  for every  $x_i$ , and  $\mathbf{C}$  the covariance matrix with elements  $\mathbf{C}_{ii'} = E(x_i x_{i'}) - \mu_i \mu_{i'}$ , and

$$(a|b) = 4\mathcal{R} \left[ \int_0^\infty \frac{\tilde{a}(f)\tilde{b}(f)}{\mathcal{N}} df \right], \quad (6.3)$$

with  $\mathcal{R}[\ ]$  the real part, and  $\mathcal{N}$  the power spectral density as given in equation 6.1.

#### 6.1.4 Signal to Noise Ratio

Another very useful definition is the so called *signal to noise ratio* (SNR). The observational data  $\vec{d}$  can be written as a linear sum of the noise  $\vec{n}$  and a gravitational wave signal  $\vec{h}(\vec{\theta})$ , or

$$\vec{d} = \vec{n} + \vec{h}(\vec{\theta}).$$

The SNR tells us how much of our data  $\vec{d}$  consists of the signal  $\vec{h}(\vec{\theta})$ . It is defined as [39]

$$\text{SNR} = \frac{(\vec{h}(\vec{\theta})|\vec{d})}{(\vec{d}|\vec{d})^{1/2}}. \quad (6.4)$$

As stated before, during this thesis, no extra noise is included during the simulations. This means that  $\vec{n} = \vec{0}$ , and thus  $\vec{d} = \vec{h}(\vec{\theta})$ , and thus that

$$\text{SNR} = (\vec{h}(\vec{\theta})|\vec{h}(\vec{\theta}))^{1/2} = 2\mathcal{R} \left[ \int_0^\infty \frac{\tilde{h}(f)^2}{\mathcal{N}} df \right]^{1/2}, \quad (6.5)$$

with  $\mathcal{R}[\ ]$  the real part, and  $\mathcal{N}$  the power spectral density as given in equation 6.1.

In this thesis, three detectors are used. When a wave is detected by multiple detectors, the SNR of this event is added quadratically:

$$\text{SNR}_{\text{tot}} = \sqrt{\sum_i \text{SNR}_i^2}$$

## 6.2 Bayes' theorem

In this subsection, we follow section II of [40], where a more thorough treatment of the subject can be found.

The way which parameters of the objects that generated gravitational waves are extracted, is via hypothesis testing. Very crudely said, this means comparing the probabilities that a wave is in the strain when a certain value of a parameter is taken and from this derive probability distributions for the value of every parameter.

This is done via Bayesian inference, in which Bayes' theorem stands central. In the context of this thesis, it is given by the equation

$$P(\mathcal{H}_i|\vec{d}, I) = \frac{P(\mathcal{H}_i|I)P(\vec{d}|\mathcal{H}_i, I)}{\sum_i P(\vec{d}|I)}, \quad (6.6)$$

where  $P(A|B)$  is the probability of  $A$  being true if  $B$  is true,  $\vec{d}$  is the observational data,  $I$  is the prior information, and  $\mathcal{H}_i$  is the model or hypothesis. In the context of this thesis,  $\mathcal{H}_i$  is either

the gravitational wave model as described in section 4.3, or the hypothesis that the data consists of pure noise. These priors are a probability distributions and boundaries for every parameter within the model. More information about these priors is given in section 7.1.

A very helpful way of comparing between two different models, is via the so called *Bayes factor*: the ratio  $O_{ij}$  between the probabilities of two different models  $\mathcal{H}_i$  and  $\mathcal{H}_j$  is given by

$$\mathcal{O}_{ij} = \frac{P(\mathcal{H}_i|I)P(\vec{d}|\mathcal{H}_i, I)}{P(\mathcal{H}_j|I)P(\vec{d}|\mathcal{H}_j, I)} \equiv \frac{P(\mathcal{H}_i|I)}{P(\mathcal{H}_j|I)} B_{ij}, \quad (6.7)$$

with  $B_{ij}$  the Bayes factor. One can take the Bayes factor to be between the hypothesis  $\mathcal{H}_i$  that a gravitational wave of a particular model is present, and the hypothesis  $\mathcal{H}_j$  that the data is just pure noise. This way, if the data is more likely just pure noise, we end up with  $B_{ij} < 1$ . We will use this to confirm the validity of our results.

### 6.3 How to estimate parameters

Our model  $\mathcal{H}$  contains a set of parameters  $\vec{\theta}$ . In this thesis, our waveform models have between 11 and 14 parameters. We will take a look at the exact parameters in section 7.1, but for now it suffices to understand that these parameters define the system from which the gravitational waves originated, such as masses.

These parameters are computed via the likelihood that the gravitational wave data  $\vec{d}$  fits the model  $\mathcal{H}_i$ : if the model using the parameters  $\vec{\theta}$  fits the data best, these values for the parameters must be the true values. We call this probability of  $\vec{d}$  fitting the model  $\mathcal{H}$  the *evidence*, which is given by

$$Z = P(\vec{d}|\mathcal{H}, I) = \int_{\Theta} p(\vec{\theta}|\mathcal{H}, I) p(\vec{d}|\mathcal{H}, \vec{\theta}, I) d\vec{\theta}, \quad (6.8)$$

where  $\Theta$  is the full parameter space. It is clear that this integral is between 11 and 14 dimensional, and thus analytically unsolvable. This is done numerically via specialised computer clusters, where this can still be a matter of months until a result is obtained.

The final result for all the parameters  $\vec{\theta}$  is a probability function, also called the *posterior density function* or just *posterior*, given by

$$p(\vec{\theta}|\vec{d}, \mathcal{H}, I) = \frac{p(\vec{\theta}|\mathcal{H}, I) p(\vec{d}|\vec{\theta}, \mathcal{H}, I)}{p(\vec{d}|\mathcal{H}, I)}.$$

The posterior of a single parameter  $\theta_A$  depends on all other parameters  $\vec{\theta}_B$ , where  $\vec{\theta} = \{\theta_A, \vec{\theta}_B\}$  and  $\Theta_B$  is the parameter space of all parameters  $\vec{\theta}_B$ . It can be shown that this posterior is given by

$$p(\vec{\theta}_A|\vec{d}, \mathcal{H}, I) = \int_{\Theta_B} p(\vec{\theta}|\vec{d}, \mathcal{H}, I) d\vec{\theta}_B. \quad (6.9)$$

For a hypothesis where a signal is present, the probability function  $p(\vec{d}|\vec{\theta}, \mathcal{H}, I)$  is given by a Gaussian distribution function like equation 6.2, substituting  $\vec{d}$  for  $\vec{x}$ , and setting  $\vec{\mu} = \vec{h}(\vec{\theta})$ . If we have a hypothesis  $\mathcal{H}_n$  where the signal is pure noise, so  $\vec{h}(\vec{\theta}) = 0$ , the probability function  $p(\vec{d}|\vec{\theta}, \mathcal{H}, I)$  is given by the same equation, but now  $\vec{\mu} = 0$ .

In this thesis, a signal is detected by multiple detectors. The total data is given by  $\vec{d}_{\text{total}} = \{\vec{d}_1, \vec{d}_2, \dots\}$ , with every entry the observational data of a different detector. A probability of the

total data is then very easily calculated as the product

$$p(\vec{d}_{\text{total}}|\vec{\theta}, \mathcal{H}, I) = \prod_i p(\vec{d}_i|\vec{\theta}, \mathcal{H}, I).$$

### 6.3.1 Nested sampling

The *nested sampling algorithm* was first developed by Skilling[41] as a way to decrease the computation time it takes to solve the evidence of equation 6.8. The total parameter space  $\Theta$  is of course a continuous manifold: every parameter can take any value (albeit bounded), and their probability functions as given in equation 6.9 are smooth functions. In order to numerically calculate this, we approximate that the values of a parameter are finite and lie on a lattice. Every one of these points, called *live points*, is given a certain weight by a *weight function*  $\vec{w}$ . When there are a total of  $N$  live points, we can thus approximate equation 6.8 as

$$Z \approx \sum_{i=0}^{N-1} p(\vec{d}|\vec{\theta}_i, \mathcal{H}, I)w_i \equiv \sum_{i=0}^{N-1} L_i w_i, \quad (6.10)$$

where it is defined that  $w_i = p(\vec{\theta}_i|\mathcal{H}, I)d\vec{\theta}$ , and  $L_i = p(\vec{d}|\vec{\theta}_i, \mathcal{H}, I)$  is called the *likelihood*. The calculation of the weight function is what makes the nested sampling algorithm so efficient and helpful.

If we think of each likelihood  $L_i$  as lying on a contour plot of probabilities in parameter space (see the left hand side of figure 6), we can define  $X_i$  as the *prior mass* corresponding to that point. The prior mass is higher if  $L_i$  lies on a point of low probability, and is normalised to unity. We can then rewrite equation 6.10 to be equal to

$$Z \approx \sum_i L(X_i)\Delta X_i,$$

where  $\Delta X_i = X_{i+1} - X_i$ . It can be shown that to very good approximation, we can write that  $X_i \approx \exp(-i/N)$ , and the corresponding weight  $w_i = (X_{i-1} + X_{i+1})/2$ .



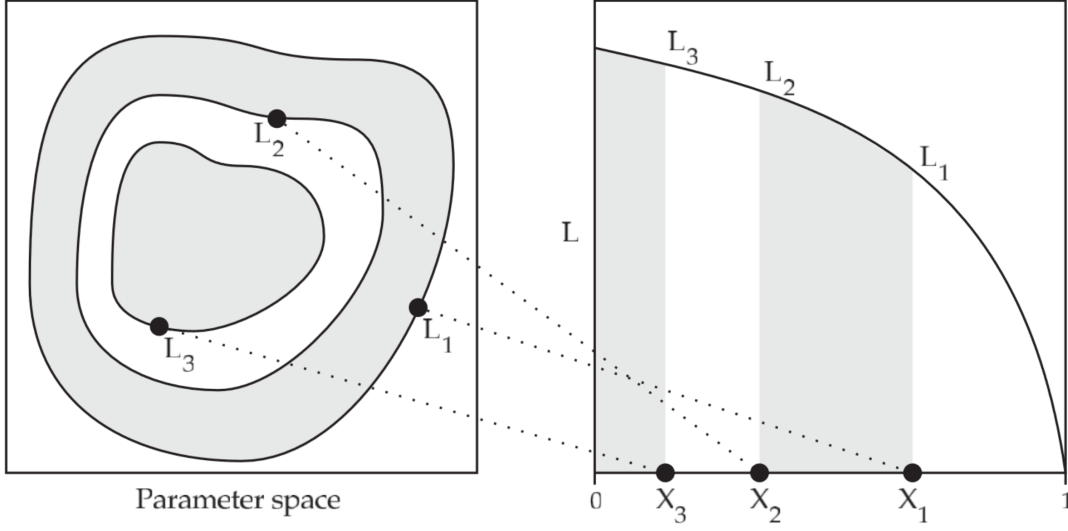


Figure 6: A visualisation of the connection between the likelihood  $L_i$  and the corresponding prior mass  $X_i$ . On the left, a contour plot of the probabilities of each likelihood is given. On the right, the corresponding weight mass is given. Adapted from figure 1 of [40].

In quasi code, the nested sampling algorithm is given by chapter 6 of [42] to be:

- Start with  $N$  points  $\vec{\theta}_0, \dots, \vec{\theta}_N$  from prior.  
Initialise  $Z = 0$  and  $X_0 = 1$ .
- Repeat for  $i = 1, \dots, j$ :  
Record the lowest of the current likelihood values as  $L_i$ , set  $X_i = \exp(-i/N)$  and set  $w_i = (X_{i-1} + X_{i+1})/2$ .  
Increment  $Z$  by  $L_i w_i$ , then replace points of lowest likelihood by new one drawn from within  $L(\vec{\theta}) > L_i$ , in proportion to the prior  $I(\theta)$ .
- Increment  $Z$  by  $N^{-1}(L(\vec{\theta}_1) + \dots + L(\vec{\theta}_N))X_j$

During the execution of the algorithm, for every point  $i$ , the value of  $L_i$ ,  $\theta_i$  and  $X_i$  is stored. Since these points are drawn from the prior distribution, we can calculate the probability density of the parameters as

$$p(\vec{\theta}_i | \mathcal{H}, I) = p(\vec{\theta}_i | \text{NS}) X_i,$$

where  $p(\theta_i | \text{NS})$  is the probability density as determined by nested sampling. Using equation 6.8, we can thus write that the probability density of  $\theta_i$  goes as

$$p(\vec{\theta}_i | \vec{d}, \mathcal{H}, I) \propto p(\vec{\theta}_i | \text{NS}) p(\vec{d} | \vec{\theta}_i, \mathcal{H}, I) X_i. \quad (6.11)$$

We can thus use nested sampling to determine the probability densities for every parameter.

## 7 Binary systems and Parameters

The gravitational waves as treated in this paper all find the same origin: two very massive objects circling around each other and, after some time, colliding and merging into one object. We treat

two of such *binary systems*: a *Binary Black Hole*, two black holes which inspiral and collide, and a *Neutron Star Black Hole* binary, consisting of a neutron star and a black hole. Gravitational waves of both these events have been observed [43] [44], and thus present real physical relevance.

## 7.1 Gravitational wave parameters

From an unlensed gravitational wave in GR, 15 parameters can be extracted [43] which tell us all about the two objects from which it originated. Not all of these parameters are used in this thesis to save time on the very long computing time, so that this research could be finished within the allotted time. We took all of our observed objects to be spin-less: this saves 6 parameters in the total (spin magnitude and orientation for both objects, and two parameters which have to do with their orientation relative to each other).

Most of the parameters are present in every theory of gravity as treated in this thesis. These are: the chirp mass  $\mathcal{M}$  as defined in equation 3.3 and the mass ratio  $q = m_2/m_1$  which define the masses of the two inspiraling objects, the right ascension  $\alpha$  and declination  $\delta$  which determine the position of the event in the sky, the luminosity distance  $d_L$  which determines the distance to the event, the time of coalescence  $t_c$  which determines when the signal entered the detectors, the phase  $\phi_0$  which is the phase at  $t_c$  as defined in section 3.3, the inclination angle  $\iota$  which is the angle between the observer and the plane on which the two inspiraling object move, and the angle  $\psi$  which determines the rotation of this inspiraling plane with respect to the observer.

Because we are looking into gravitational waves which are lensed, two more parameters enter: the magnification ratio  $\mu$  as defined in equation 5.7 and the time shift  $t_{\text{shift}}$ , which is the difference in time of arrival of the two images as defined in equation 5.5.

Finally, some extra parameters enter for non-GR theories of gravity. As can be seen in section 4.3, the Brans-Dicke theory of gravity depends on a coupling constant  $\omega_{BD}$  and the sensitivities  $s_1$  and  $s_2$  of the two colliding objects as defined in equation 4.4. The Rosen theory of gravity also depends on the sensitivities, and Lightman-Lee only depends on the difference in sensitivity  $\Delta s = s_1 - s_2$ . An overview is given below in table 7.1.

Theory of gravity	$s_1$	$s_2$	$\Delta s$	$\omega_{BD}$
GR				
Brans-Dicke	✓	✓		✓
Rosen	✓	✓		
Lightman-Lee			✓	

Table 4: The extra parameters that enter the model, based on the theory of gravity of the model.

The full list of parameters is thus given by:

$$\vec{\theta} = \{\mathcal{M}, q, \iota, \psi, \phi_0, t_c, t_{\text{shift}}, \alpha, \delta, d_L, \mu, s_1, s_2, \Delta s, \omega_{BD}\}, \quad (7.1)$$

where we set the parameters that do not enter a model to be equal to 0.

From this set of parameters, we create two separate sets of parameters, one for each wave. This is done because the frameworks upon which we work are not designed to process multiple images of the same events: we create a likelihood function which acts as a single event, but consists of two.

For the first event, we simply take the parameters as given in equation 7.1 and remove the two parameters that have to do with the lensing: the time-shift  $t_{\text{shift}}$  and magnification ratio  $\mu$ . For the second event, the wave changes as described in section 5.2. Since only the amplitude of the wave changes, but the rest stays the same, we change the luminosity distance: a weaker wave seemingly seems to have come from farther away. As can be seen in section 4.3, all gravitational waves of interest go as  $1/d_L$ , so we can simply state that  $d_{L,2} = \mu \times d_L$ : a signal that is twice as weak seems to have come from twice as far. The lensed wave also arrives at a later time of course, so we take that  $t_{c,2} = t_c + t_{\text{shift}}$ . After this, the lensing parameters are removed from the list of parameters, a likelihood function is calculated for both the first and second event, and they are combined into a single one.

Each parameter has a corresponding prior. These are probability distributions of a parameter which speed up the sampling. This is done both by the boundaries and shape of the prior. For example, the prior of the mass ratio  $q$  is taken to be between 0 and 1 since it is a ratio, the sensitivities  $s_1$  and  $s_2$  have an upper limit just above 0.5 since this is their theoretical maximum, and the luminosity distance  $d_L$  has a non-uniform distribution to reflect that the further away we move from the Earth, the more stars and black holes we encounter from which the wave might originate.

## 7.2 Binary systems

### 7.2.1 Binary Black Holes

The first of the two observed systems are so called *Binary Black Holes* (or BBH for short). These are two black holes which circle around each other, and make up the most of the observed binary systems at the LIGO-Virgo collaboration [45], and are thus of great interest. The parameters are loosely inspired on event GW150914[4][43], which was the first ever detected gravitational wave event, but some parameters were changed to create a more interesting scenario. Its sky position and mass-related parameters were taken to be the same, but we increased the luminosity distance to  $d_L = 1000 \times 10^6 \text{Mpc}$ , such that the signal would be more difficult to find in the noise. While it could be read in section 4.3 that in the event that the Brans-Dicke coupling constant  $\omega_{BD}$  exists, its value would  $> 40000$ , we chose to take a value of  $\omega_{BD} = 4$ , since trial runs indicated that for  $\omega_{BD} = 40000$ , there is no distinguishable difference between the GR and the Brans-Dicke gravitational waves. For the values of the sensitivities as defined in equation 4.4, we took the values of  $s_1 = 0.5$ ,  $s_2 = 0.3$  and thus  $\Delta s = 0.2$ . While we stated before that in the case of Black Holes, it can be observed from section 4.3 that all the alternative theories scale with the difference in sensitivities: if we take this to be zero, there simply would be no interesting results as a result. Because of this, the BBH systems are non-physical, but since the goal of this paper is a proof of concept, this is not an issue. For the lensing parameters, we took that  $\mu = 1.5$  and  $t_{\text{shift}} = 3600\text{s}$ .

### 7.2.2 Neutron Star Black Hole

The second observed system in this thesis is the *Neutron Star Black Hole* (or NSBH for short). The first gravitational wave originating from such a system was detected in 2017 [44]. This is a much more interesting case for the probing of alternative theories of gravity, because of the mass difference of the two objects: a neutron star has a mass of at most  $2.16M_\odot$  [46], while black holes have a mass of at least  $3.3M_\odot$ , although typically higher [47]. Because of this, there is a large difference in sensitivity  $\Delta s$  for the alternative theories of gravity, since it scales with mass[27].

We can thus use a physical system to still produce gravitational waves of interest.

However, since the masses of one of the two objects is significantly lower in comparison to a BBH system, the NSBH system has a relatively low chirp mass  $\mathcal{M}$ : we take a system consisting of the masses  $m_1 = 10M_\odot$  and  $m_2 = 2M_\odot$ , resulting in a chirp mass of  $\mathcal{M} \approx 3.67M_\odot$  and a mass ratio of  $q = 0.2$ . As seen in section 4.3, this will result in weaker GW's (especially for the Rosen theory of gravity), so we will place the system at a distance of  $d_L = 200$  Mpc. Since we want this system to be as physically correct as possible, we take  $s_1 = 0.5$ ,  $s_2 = 0.4$  and thus  $\Delta s = 0.1$ , in accordance with the theoretical values as posted in section 4.4. All other parameters are the same as in the BBH case.

## 8 Results

### WRITE SHORT INTRODUCTION TO THIS CHAPTER

#### 8.1 How the results are obtained

Throughout the different runs, only 2 parameters are changed: the *injected waveform* (the waveform model which is used to generate the gravitational wave), and the *sampled waveform* (the waveform model which is used to estimate the parameters). The sampler is run for every combination of these two parameters, resulting in  $4 \times 4 \times 2 = 32$  different results. For every run, the results are obtained the same way, of which we will now give a very crude overview:

- An waveform object containing the model for the injected gravitational wave is generated using the *bilby* package [19], using the injected waveform model as described in section 4.3.
- Using this waveform object, the two images of the detected gravitational wave are generated.
- These images are "injected" into the network of three detectors, that is to say, a strain is calculated for every detector, where the strain is defined in equation 4.2. Since the first image and second image arrive at a different time, we end up with 6 different strains.
- A second waveform object is generated, this time using the waveform which is to be used by the sampler.
- The priors for every parameter are generated for the sampler, based on the sampled waveform.
- Using the 6 different strains, priors and waveform object containing the sampled waveform, a combined likelihood function is calculated.
- The likelihood function and priors are handed to the *pymultinest* sampler [48], which calculates the likelihood for the sampled waveform.

#### 8.2 Bayes factors

First, we take a look at the results from all 32 runs combined. Below in table ??, we have the logarithmic Bayes factors  $\log(B)$  for every run. We will draw some quick conclusions from this table, then move on to every individual system for more in depth discussion. Firstly, notice that

for every case, there is nearly no difference in the logarithmic Bayes factor for General Relativity and the Brans-Dicke theory of gravity. Why this is, we will continue to look into in the next section. Secondly, the signal for Rosen is always very weak: it consistently has the lowest Bayes factors when it is not the injected waveform, and when it is, the logarithmic Bayes factors are very low in comparison to other runs using the same system. When the Rosen wave was injected into the NSBH system, all the values for  $\log(B)$  were below zero: this indicates that the sampler deems it more likely that the strain is just pure noise, and thus that no signal was found. Lastly, we notice that the BD and GR theories, when the sampled waveforms, always return values of  $\log(B)$  which are very close to one another. When we take a look at the uncertainties in the values of  $\log(B)$  due to random events [40], we find that these are in the order of  $10^{-1}$ , and thus that the values of sampled BD and GR waves do not differ significantly.

Waveform	BBH	NSBH
GR-GR	235.62	482.29
GR-BD	236.21	482.14
GR-LL	173.37	6.44*
GR-Rosen	16.72	-0.70
BD-GR	192.67	398.31
BD-BD	193.11	398.58
BD-LL	138.67	2.04*
BD-Rosen	11.67	-0.71
LL-GR	52.66	-1.25
LL-BD	53.05	-1.23
LL-LL	602.43	916.54*
LL-Rosen	24.98	-0.66
Rosen-GR	-2.62	-1.33
Rosen-BD	-2.55	-1.32
Rosen-LL	32.49	-2.27*
Rosen-Rosen	40.28	-0.70

Table 5: The logarithmic Bayes factors  $\log(B)$  for every run, as defined in equation 6.7, where every value listed has an uncertainty in the order of  $10^{-1}$ . The naming convention of the runs is that first, the injected waveform model is named, separated by a dash from the sampled waveform model. The values marked with a \* are from runs where the sampler hasn't fully converged, but were far enough done for it to be a very good indication.

## 8.3 Results per system

### 8.3.1 Binary Black Hole

We will take a look at the Binary Black Hole system as described in section 7.2.1. Of particular interest are the runs where the sampled waveform is the same as the injected waveform. For these we will take a look at the parameters as calculated by the sampler. This gives us a sense for the correlation between the Bayes factor  $B$  as defined in equation 6.7, and the accuracy of the calculated parameters. The results are given in the form of a probability distribution for the value of the parameter, which are included in a series of corner plots. For illustrative purposes,

the plots of the Lightman-Lee run for the BBH system with no noise is included in the appendix. The results are below in table 6.

Parameters:	Injected Value	GR	BD	LL	Rosen
$\mathcal{M}(M_{\odot})$	28.25	$28.29^{+0.10}_{-0.14}$	$28.34^{+0.09}_{-0.13}$	$28.38^{+0.04}_{-0.06}$	$28.09^{+0.36}_{-0.74}$
$q$	0.84	$0.86^{+0.09}_{-0.08}$	$0.89^{+0.07}_{-0.08}$	$0.96^{+0.02}_{-0.03}$	$0.78^{+0.14}_{-0.17}$
$\iota(\text{rad})$	0.79	$0.55^{+0.27}_{-0.25}$	$0.58^{+0.25}_{-0.26}$	$0.79^{+0.07}_{-0.06}$	$0.68^{+0.33}_{-0.31}$
$\psi(\text{rad})$	2.659	$2.00^{+0.84}_{-1.58}$	$2.10^{+0.76}_{-1.67}$	$2.66^{+0.08}_{-0.09}$	$1.21^{+1.06}_{-0.54}$
$\phi_0(\text{rad})$	0	$3.84^{+1.88}_{-3.12}$	$3.89^{+1.86}_{-3.23}$	$0.15^{+6.08}_{-0.11}$	$3.79^{+1.61}_{-3.00}$
$t_c(\text{s})$	100000	$100000^{+0.00}_{-0.00}$	$100000^{+0.00}_{-0.00}$	$100000^{+0.00}_{-0.00}$	$100000^{+0.00}_{-0.00}$
$t_{\text{shift}}(\text{s})$	3600	$3600^{+0.00}_{-0.00}$	$3600^{+0.00}_{-0.00}$	$3600^{+0.00}_{-0.00}$	$3600^{+0.00}_{-0.00}$
$\alpha(\text{rad})$	1.375	$1.39^{+0.13}_{-0.12}$	$1.39^{+0.14}_{-0.13}$	$1.37^{+0.06}_{-0.05}$	$1.42^{+0.34}_{-0.30}$
$\delta(\text{rad})$	-1.2108	$-1.21^{+0.01}_{-0.01}$	$-1.21^{+0.02}_{-0.01}$	$-1.21^{+0.01}_{-0.01}$	$-1.20^{+0.04}_{-0.03}$
$d_L(10^6\text{Mpc})$	1000	$1179.12^{+151.50}_{-205.35}$	$1267.01^{+179.02}_{-212.38}$	$1009.84^{+31.65}_{-31.32}$	$1159.44^{+256.46}_{-249.01}$
$\mu$	1.5	$1.55^{+0.16}_{-0.14}$	$1.55^{+0.17}_{-0.15}$	$1.50^{+0.09}_{-0.09}$	$1.77^{+0.57}_{-0.36}$
$s_1$	0.5		$0.40^{+0.10}_{-0.10}$		$0.47^{+0.04}_{-0.11}$
$s_2$	0.3		$0.40^{+0.10}_{-0.10}$		$0.46^{+0.05}_{-0.11}$
$\Delta s$	0.2			$0.20^{+0.00}_{-0.00}$	
$\omega_{BD}$	4		$24776.57^{+16620.57}_{-16370.82}$		
SNR-1		20.11	18.43	30.50	11.10
SNR-2		12.07	11.08	19.98	5.20
$\text{Log}(B)$		235.62	193.11	602.43	40.28

Table 6: The estimated parameters for every model using the same injected and sampled waveform for the BBH system. The parameters are as defined in section 7.1, their uncertainties are a  $1-\sigma$  confidence interval. SNR-1 is the signal to noise ratio as defined in equation 6.5 of the first image, SNR-2 of the second image.  $\text{Log}(B)$  is the logarithm of the Bayes factor as defined in equation 6.7, taken between the model  $\mathcal{H}$  and the noise. When no value for a parameter is given, the parameter is not present in that theory of gravity. Note that some parameters are periodic:  $\iota$  and  $\psi$  are periodic between 0 and  $\pi$ ,  $\alpha$  and  $\delta$  are periodic between  $-\pi$  and  $\pi$ , and  $\phi_0$  is periodic between 0 and  $2\pi$ . Because of this, a value might seem to be determined very inaccurately when in reality it is not.

It might feel logical that since no noise was added, the SNR should potentially infinite. However, per construction in equation 6.5, it is not, and still is a useful number which indicated how well the signal is defined in the detectors. While SNR is thus a bit of a misnomer in this case, we will stick with it due to convention.

When we look at the relation between the SNRs and the Bayes factor  $B$ , a very simple relation between the two becomes clear: the higher the SNR, the better the sampler can determine the

correctness of the model, and thus results in a higher  $B$ . The differences in SNR (and thus  $B$ ) come from the differences in amplitude of the different gravitational waves: as can be seen in section 4.3, the waves created by Lightman-Lee just have a larger amplitude than Rosen gravitational waves. The SNR of 5.20 of the second Rosen image is even lower than the conventional threshold of 7 or 8 for detecting an event[40], and might thus not even be noticed under real circumstances when even more noise is added. We also see that the higher the Bayes factor  $B$ , the better the parameters are calculated.

Over all, the sampler was able to very accurately determine the parameters for every model, except for the Brans-Dicke model. Here, the coupling constant is calculated to be  $\omega_{BD} \approx 24777$ , with errors in the same order of magnitude. If we fill in this value of  $\omega_{BD}$  into the model, we see that this is essentially the GR-limit case of Brans-Dicke theory: the cross and plus polarisations become indistinguishable from the GR polarisations, and the breathing polarisation disappears. Because of this, the sampler actually calculates the wave to be a GR waveform. As we can see from the plots in figure 7, there is only a significant difference between GR and BD for  $\omega_{BD} \lesssim 10$ . Because prior of  $\omega_{BD}$  was taken to be very large to also include the "real" value of  $\omega_{BD} \approx 40.000$  [29], the sampler most likely did not have the resolution to find these values, and found no difference in waveforms when it changed  $\omega_{BD}$ : hence the very large uncertainty. Because the sampler was basically working in the GR-limit of BD theory, the calculated values for the sensitivities  $s_1$  and  $s_2$  are also very badly returned: these are taken to be  $0.4 \pm 0.1$ , which is just a flat probability distribution between the borders of the prior of 0.35 and 0.55, meaning the sampler cannot find any difference in the wave when it changes these values. Concluding from this, even for extremely low values of  $\omega_{BD} = 4$ , the sampler seemingly cannot distinguish between General Relativity and Brans-Dicke.

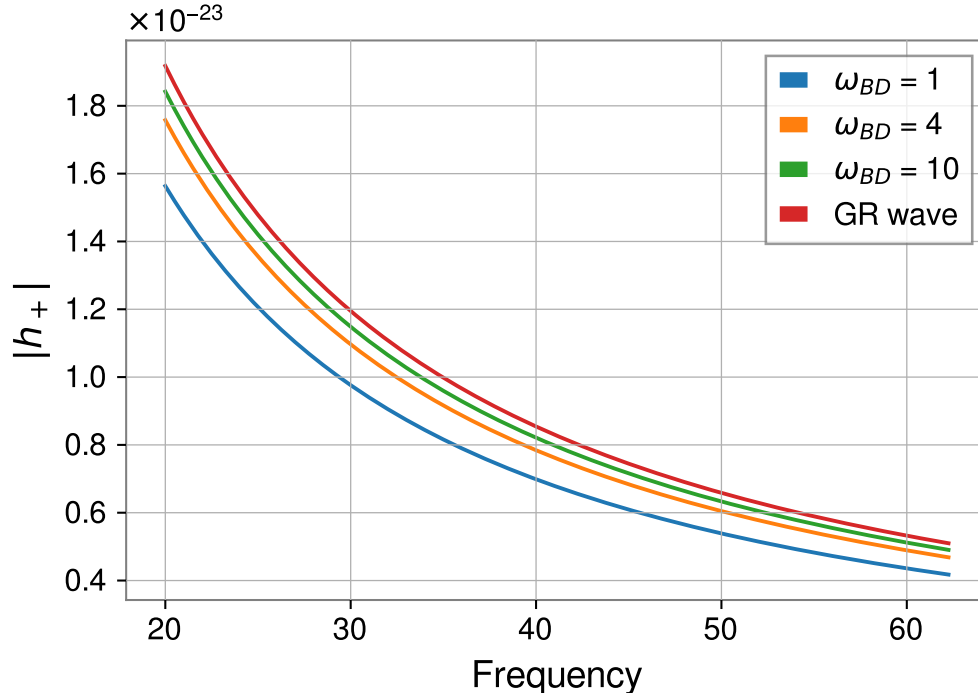


Figure 7: The amplitude of the plus-polarisation  $|h_+|$  of the Brans-Dicke wave for the parameters of the BBH system as defined in section 7.2.1 for different values of the Brans-Dicke coupling constant  $\omega_{BD}$ . In red:  $|h_+|$  for the GR wave of the same BBH system.

Below in table 7, we can see the Bayes factors for this system, but comparing the hypothesis of the injected wave model with another wave model. From the definition of the Bayes factor in equation 6.7, it is clear to see that we can simply use the relation

$$\log(B_{is}) = \log(B_{in}) - \log(B_{sn}) \quad (8.1)$$

where  $B_{is}$  is the Bayes factor between the injected and sampled wave model,  $B_{in}$  is the Bayes factor between the injected wave model hypothesis and the noise hypothesis, and  $B_{sn}$  is the Bayes factor between the sampled wave model and the noise hypothesis. We can thus easily subtract the values in table 5 from each other to compare how much better a model fits the signal.



	GR	BD	LL	Rosen
GR	0	-0.95	61.89	218.54
BD	0.44	0	54.44	181.44
LL	549.77	549.38	0	577.45
Rosen	42.90	42.83	7.79	0

Table 7: The logarithm of the relative Bayes factor  $\log(B_{is})$  as defined in equation 8.1 for the BBH model, where every value listed has an uncertainty in the order of  $10^{-1}$ . The injected models are places on the row above, the sampled waveforms on the column to the left. Note that  $\log(B_{is}) < 0$  indicates that the signal is deemed more likely to be the sampled wave model than the injected wave model.

From the relative logarithmic Bayes factors, we can immediately notice again that the difference between General Relativity and Brans-Dicke is very small indeed, and do not differ significantly due to the uncertainties in the Bayes factors [40]. We also notice the very high Bayes factors when we inject using Lightman-Lee. This can be explained from the fact that for this set of runs, the SNR was very high, and thus the wave was very clearly defined, allowing the sampler to see a clear distinction between the waveform models.

The relatively small difference between LL and Rosen when the Rosen wave is injected ( a value of 7.79) is strange, since the difference between Rosen and LL when LL is injected is so large (577.45). This is again most likely due to the high difference in SNR, and thus how badly the Rosen wave is defined in the detectors.

Lastly, the sampler is able to very distinctly pick out LL when it is injected, and while it sees GR and BD to be the same, it is able to differentiate between these two and LL and Rosen when GR and BD are injected. The high values for  $B$  when LL is injected are again easily explained when we look at the SNR: because it is so high for the LL injection cases (it only depends on the injected wave, and is thus the value from table 6 is the same for all LL injections of this system), the waveform is very clearly defined in the detectors, and thus can be easily distinguished.

### 8.3.2 Neutron Star Black Hole

We will now turn our attention to the NSBH system as defined in section 7.2.2. First, we once more look at the full results from the "correct" runs: where the injected and sampled wave model are the same. These results are shown in table 8 below.

Parameters:	Injected Value	GR	BD	LL*	Rosen
$\mathcal{M}(M_\odot)$	3.67	$3.67^{+0.00}_{-0.00}$	$3.68^{+0.00}_{-0.00}$	$3.67^{+0.00}_{-0.00}$	$3.90^{+3.35}_{-2.00}$
$q$	0.20	$0.20^{+0.01}_{-0.01}$	$0.20^{+0.02}_{-0.01}$	$0.20^{+0.00}_{-0.00}$	$0.56^{+0.28}_{-0.28}$
$\iota(\text{rad})$	0.79	$0.51^{+0.24}_{-0.24}$	$0.52^{+0.25}_{-0.24}$	$0.72^{+0.06}_{-0.05}$	$1.55^{+0.57}_{-0.57}$
$\psi(\text{rad})$	2.659	$1.84^{+0.96}_{-1.35}$	$2.15^{+0.67}_{-1.69}$	$2.71^{+0.03}_{-0.03}$	$1.58^{+1.07}_{-1.08}$
$\phi_0(\text{rad})$	0	$3.43^{+2.22}_{-2.73}$	$4.20^{+1.51}_{-3.42}$	$6.11^{+0.04}_{-0.09}$	$3.09^{+2.18}_{-2.10}$
$t_c(\text{s})$	100000	$100000^{+0.00}_{-0.00}$	$100000^{+0.00}_{-0.00}$	$100000^{+0.00}_{-0.00}$	$99999.99^{+0.64}_{-0.63}$
$t_{\text{shift}}(\text{s})$	3600	$3600^{+0.00}_{-0.00}$	$3600^{+0.00}_{-0.00}$	$3600^{+0.00}_{-0.00}$	$3599.99^{+0.32}_{-0.31}$
$\alpha(\text{rad})$	1.375	$1.38^{+0.04}_{-0.04}$	$1.38^{+0.04}_{-0.04}$	$1.33^{+0.01}_{-0.02}$	$3.15^{+2.16}_{-2.12}$
$\delta(\text{rad})$	-1.2108	$-1.21^{+0.00}_{-0.00}$	$-1.21^{+0.01}_{-0.00}$	$-1.21^{+0.00}_{-0.00}$	$0.00^{+0.69}_{-0.67}$
$d_L(10^6\text{Mpc})$	200	$239.55^{+24.17}_{-34.93}$	$260.33^{+28.00}_{-39.64}$	$200.73^{+4.20}_{-3.75}$	$3832.68^{+750.38}_{-1076.29}$
$\mu$	1.5	$1.53^{+0.11}_{-0.10}$	$1.53^{+0.12}_{-0.11}$	$1.47^{+0.05}_{-0.05}$	$2.89^{+1.33}_{-1.43}$
$s_1$	0.5		$0.40^{+0.10}_{-0.10}$		$0.39^{+0.10}_{-0.09}$
$s_2$	0.4		$0.40^{+0.10}_{-0.10}$		$0.39^{+0.10}_{-0.09}$
$\Delta s$	0.1			$0.09^{+0.00}_{-0.00}$	
$\omega_{BD}$	4		$24882.97^{+167594.38}_{-16663.25}$		
SNR-1		28.05	25.77	37.57	16.93
SNR-2		16.93	15.581	25.17	8.41
$\text{Log}(B)$		482.29	398.58	916.54	-0.70

Table 8: The estimated parameters for every model using the same injected and sampled wave model for the NSBH system. The parameters are as defined in section 7.1, their uncertainties are a  $1-\sigma$  confidence interval. SNR-1 is the signal to noise ratio as defined in equation 6.5 of the first image, SNR-2 of the second image.  $\text{Log}(B)$  is the logarithm of the Bayes factor as defined in equation 6.7, taken between the model  $\mathcal{H}$  and the noise. When no value for a parameter is given, the parameter is not present in that theory of gravity. Note that some parameters are periodic:  $\iota$  and  $\psi$  are periodic between 0 and  $\pi$ ,  $\alpha$  and  $\delta$  are periodic between  $-\pi$  and  $\pi$ , and  $\phi_0$  is periodic between 0 and  $2\pi$ . Because of this, a value might seem to be determined very inaccurately when in reality it is not. Lightman-Lee is marked with a star, as this run had not yet fully converged, but far enough for it to be included.

As in the BBH case, we again see that the Brans-Dicke coupling constant  $\omega_{BD}$  is very badly returned: just like before its value and uncertainties indicate that probability distribution function is just the flat prior, and the sampler thus sees the BD model as in its GR limit. This is further demonstrated by the fact that  $s_1$  and  $s_2$  are again returned exactly as their prior, since the BD model does not depend on  $s_1$  and  $s_2$  in its GR limit.

The parameters for GR and Lightman Lee are returned very well, as to be expected by their high SNR's. The Lightman Lee wave is defined so well in fact, that the sampler is able to es-

timate several parameters as the correct values with no significant uncertainty, even though the sampler wasn't done yet. This is reflected in the very high logarithmic Bayes factors for both these runs.

The same can't be said for the Rosen wave: It has a  $\log(B)$  lower than 0. This indicates that no signal was found, since the sampler thinks the strain measured is just pure noise. This is a very weird result: while the SNRs are undeniably lower compared to the other cases, they are still a lot higher than the conventional threshold of  $\text{SNR} = 8$  [40], and higher than the BBH system where a signal was found. We are unsure of the reason of this result, and recommend further research to be done, since we assume this to be an error. Since no other discrepancies are found in the results, we consider this to be an error isolated to the Rosen injection in the NSBH system, and see no reason to doubt the validity of our other results.

We will now look at the Bayes factors comparing the different hypotheses as defined in equation 8.1. The results of these comparisons are placed in table 9 below.

	GR	BD	LL	Rosen
GR	0	0.15	475.85*	482.99
BD	0.27	0	396.54*	399.29
LL	917.79*	917.77*	0	917.20*
Rosen	x	x	x	x

Table 9: The logarithm of the relative Bayes factor  $\log(B_{is})$  as defined in equation 8.1 for the BBH model, where every value listed has an uncertainty in the order of  $10^{-1}$ . The injected models are placed on the row above, the sampled waveforms on the column to the left. Note that  $\log(B_{is}) < 0$  indicates that the signal is deemed more likely to be the sampled wave model than the injected wave model. The crosses in the row corresponding to the Rosen injection indicate that the authors deem these results invalid, and thus no interpretation to them will be given. The values marked with a \* indicate that the calculated value involves a Bayes factor from a run that has not fully converged yet. While these values give a very good indication of the true value, it might differ.

We once again see that the sampler does not find a significant difference between GR and Brans-Dicke. The sampler is however able to clearly distinguish between the two and LL and Rosen, where the high Bayes factors are to be expected due to the high SNRs of the runs. Lightman-Lee is also very clearly distinguishable by the sampler, even though as indicated the runs were not complete. The reason behind the runs not being complete is most likely also found in the high SNR of the Lightman-Lee injection: since the waveform is so clearly defined, it can determine the parameters to a very high accuracy, but this takes a lot of computing time (more than 9 days to be exact).

The Rosen injections are indicated with a cross, this is as to indicate that the authors deem these results invalid, and improper to perform an analysis of this data. Apart from this, no further difference with the BBH system was found.

## 9 Conclusion

For this thesis, a framework was developed to combine the two detections of a lensed gravitational wave and perform statistical analysis over them, in order to distinguish between multiple theories of gravity. As a proof of concept and to demonstrate this framework, four theories of gravity were selected, with which lensed gravitational waves were simulated from both a Binary Black Hole and Neutron Star Black Hole merger. These waves were then combined using the framework and it was analysed how well they could be distinguished from each other.

Of these four theories of gravity, the framework was able to distinguish very clearly between General Relativity and the theories which do not contain a limit in which General Relativity is reached. It was not able to distinguish between General Relativity and the Brans-Dicke theory of gravity. We deem this to be due both to a resolution problems of the prior for the parameter concerning the difference between Brans-Dicke and General Relativity, and the very small difference between Brans-Dicke and General Relativity in general.

The results contain discrepancies for the Rosen theory of gravity. The authors were unable to find out why this was the case, and thus recommend further research to be done into why this happened. Furthermore, due to time constraints, the simulations were not able to be done using simulated noise. The authors recommend the framework to be tested using this noise, to demonstrate the framework works under less-ideal and more realistic circumstances.

## Acknowledgements

The primary author would like to offer his most cordial gratitude to everyone who supported him during this thesis. To my daily supervisor Haris, who was my primary source of help, feedback and information, and without who this project simply wouldn't have been possible. To my supervisor Chris, whose seemingly unending knowledge on the subject helped me tremendously in very vaguely understanding those ripples of space-time. To everyone in the gravitational wave group at the UU who in one way or another helped me during this thesis. To my parents and brother, who have always been there for me during this half year. To Renske, with who I shared many a day of working on our research and was always available to exchange frustration and jokes when the project was not going the right way or I managed to nearly break yet another very expensive computer farm. To A. Leeuwte Kamermans, for his support during the writing of this thesis. And last but not least, to all my very dear friends, who all helped helped me stay sane during these sometimes trying times.

## References

- [1] Albert Einstein. “Die Grundlage der allgemeinen Relativitätstheorie”. In: *Annalen der Physik* 354.7 (1916), pp. 769–822. doi: [10.1002/andp.19163540702](https://doi.org/10.1002/andp.19163540702).
- [2] Albert Einstein. “Näherungsweise Integration der Feldgleichungen der Gravitation”. In: *Sitzungsberichte der Königlich Preussischen Akademie der Wissenschaften (Berlin)* (Jan. 1916), pp. 688–696. doi: [10.1002/3527608958.ch7](https://doi.org/10.1002/3527608958.ch7).
- [3] Maurice Ebison. ‘Subtle is the Lord ...’: *The Science and the Life of Albert Einstein*. Vol. 34. 2. IOP Publishing, Feb. 1983, pp. 76–76. doi: [10.1088/0031-9112/34/2/025](https://doi.org/10.1088/0031-9112/34/2/025).
- [4] B. P. Abbott et al. “Observation of Gravitational Waves from a Binary Black Hole Merger”. In: *Phys. Rev. Lett.* 116 (6 Feb. 2016), p. 061102. doi: [10.1103/PhysRevLett.116.061102](https://doi.org/10.1103/PhysRevLett.116.061102).
- [5] The Royal Swedish Academy of Sciences. *Press release: The Nobel Prize in Physics 2017*. URL: <https://www.nobelprize.org/uploads/2018/06/press-40.pdf>.
- [6] C. Brans and R. H. Dicke. “Mach’s Principle and a Relativistic Theory of Gravitation”. In: *Phys. Rev.* 124 (3 Nov. 1961), pp. 925–935. doi: [10.1103/PhysRev.124.925](https://doi.org/10.1103/PhysRev.124.925).
- [7] Alan P. Lightman and David L. Lee. “New Two-Metric Theory of Gravity with Prior Geometry”. In: *Phys. Rev. D* 8 (10 Nov. 1973), pp. 3293–3302. doi: [10.1103/PhysRevD.8.3293](https://doi.org/10.1103/PhysRevD.8.3293).
- [8] N. Rosen. “General Relativity and Flat Space. I”. In: *Phys. Rev.* 57 (2 Jan. 1940), pp. 147–150. doi: [10.1103/PhysRev.57.147](https://doi.org/10.1103/PhysRev.57.147).
- [9] N. Rosen. “General Relativity and Flat Space. II”. In: *Phys. Rev.* 57 (2 Jan. 1940), pp. 150–153. doi: [10.1103/PhysRev.57.150](https://doi.org/10.1103/PhysRev.57.150).
- [10] Srashti Goyal et al. “Testing the nature of gravitational-wave polarizations using strongly lensed signals”. In: *Phys. Rev. D* 103 (2 Jan. 2021), p. 024038. doi: [10.1103/PhysRevD.103.024038](https://doi.org/10.1103/PhysRevD.103.024038).
- [11] Massimo Meneghetti. *Introduction to Gravitational Lensing*. Springer International Publishing, 2021. ISBN: 978-3-030-73581-4. doi: [10.1007/978-3-030-73582-1](https://doi.org/10.1007/978-3-030-73582-1).
- [12] Arthur B. Congdon and Charles R. Keeton. *Principles of Gravitational Lensing: Light Deflection as a Probe of Astrophysics and Cosmology*. Springer International Publishing, 2018. ISBN: 978-3-030-02122-1. doi: [10.1007/978-3-030-02122-1\\_3](https://doi.org/10.1007/978-3-030-02122-1_3).
- [13] Bernard Schutz. *A First Course in General Relativity*. Second. Cambridge University Press, 2009. doi: [10.1017/CB09780511984181](https://doi.org/10.1017/CB09780511984181).
- [14] Barbara Ryden. *Introduction to Cosmology*. 2nd ed. Cambridge University Press, 2016. doi: [10.1017/9781316651087](https://doi.org/10.1017/9781316651087).
- [15] M. K. Haris. “Gravitational wave multi-detector schemes for compact binary coalescence search”. PhD thesis. School of Physics, Indian Institute of Science Education and Research, Thiruvananthapuram, Kerala, India, Oct. 2016.
- [16] Karl Schwarzschild. “Über das Gravitationsfeld eines Massenpunktes nach der Einsteinschen Theorie”. In: *Sitzungsberichte der Königlich Preussischen Akademie der Wissenschaften (Berlin)* (Jan. 1916), pp. 189–196.
- [17] Eugene Hecht. *Optics*. Fifth. Pearson, 2017. ISBN: 1-292-09693-4. doi: [10.1017/CB09780511984181](https://doi.org/10.1017/CB09780511984181).
- [18] LIGO Caltech. *Facts*. URL: <https://www.ligo.caltech.edu/page/facts>.
- [19] Gregory Ashton et al. “Bilby: A User-friendly Bayesian Inference Library for Gravitational-wave Astronomy”. In: *The Astrophysical Journal Supplement Series* 241.2 (Apr. 2019), p. 27. doi: [10.3847/1538-4365/ab06fc](https://doi.org/10.3847/1538-4365/ab06fc).

- [20] Clifford M. Will. “The Confrontation between General Relativity and Experiment”. In: *Living Reviews in Relativity* 9.1 (Mar. 2006). ISSN: 1433-8351. DOI: [10.12942/lrr-2006-3](https://doi.org/10.12942/lrr-2006-3).
- [21] C. van den Broeck. *Lecture notes for the course “Gravitational waves (NS-374B)”*, Bachelor of Physics, Utrecht University. URL: <https://www.nikhef.nl/~vdbroeck/Utrecht/>.
- [22] Curt Cutler and Éanna E. Flanagan. “Gravitational waves from merging compact binaries: How accurately can one extract the binary’s parameters from the inspiral waveform?”. In: *Phys. Rev. D* 49 (6 Mar. 1994), pp. 2658–2697. DOI: [10.1103/PhysRevD.49.2658](https://doi.org/10.1103/PhysRevD.49.2658).
- [23] Katerina Chatziioannou, Nicolás Yunes and Neil Cornish. “Model-independent test of general relativity: An extended post-Einsteinian framework with complete polarization content”. In: *Phys. Rev. D* 86 (2 July 2012), p. 022004. DOI: [10.1103/PhysRevD.86.022004](https://doi.org/10.1103/PhysRevD.86.022004).
- [24] Serge Droz et al. “Gravitational waves from inspiraling compact binaries: Validity of the stationary-phase approximation to the Fourier transform”. In: *Phys. Rev. D* 59 (12 May 1999), p. 124016. DOI: [10.1103/PhysRevD.59.124016](https://doi.org/10.1103/PhysRevD.59.124016).
- [25] Wei-Tou Ni. “Metric Theories Of Gravity and their Astrophysical Implications”. PhD thesis. California Institute of Technology, Sept. 1973. DOI: [10.7907/MCQM-3M81](https://doi.org/10.7907/MCQM-3M81).
- [26] Atsushi Nishizawa et al. “Probing nontensorial polarizations of stochastic gravitational-wave backgrounds with ground-based laser interferometers”. In: *Phys. Rev. D* 79 (8 Apr. 2009), p. 082002. DOI: [10.1103/PhysRevD.79.082002](https://doi.org/10.1103/PhysRevD.79.082002).
- [27] Clifford M. Will and Helmut W. Zaglauer. “Gravitational Radiation, Close Binary Systems, and the Brans-Dicke Theory of Gravity”. In: 346 (Nov. 1989), p. 366. DOI: [10.1086/168016](https://doi.org/10.1086/168016).
- [28] Helmut W. Zaglauer. “Neutron Stars and Gravitational Scalars”. In: 393 (July 1992), p. 685. DOI: [10.1086/171537](https://doi.org/10.1086/171537).
- [29] Justin Alsing et al. “Gravitational radiation from compact binary systems in the massive Brans-Dicke theory of gravity”. In: *Phys. Rev. D* 85 (6 Mar. 2012), p. 064041. DOI: [10.1103/PhysRevD.85.064041](https://doi.org/10.1103/PhysRevD.85.064041).
- [30] Isaac C. F. Wong et al. *Null-stream-based Bayesian Unmodeled Framework to Probe Generic Gravitational-wave Polarizations*. 2021. arXiv: [2105.09485](https://arxiv.org/abs/2105.09485).
- [31] Jacob D. Bekenstein and Robert H. Sanders. “Gravitational Lenses and Unconventional Gravity Theories”. In: 429 (July 1994), p. 480. DOI: [10.1086/174337](https://doi.org/10.1086/174337). arXiv: [astro-ph/9311062](https://arxiv.org/abs/astro-ph/9311062) [[astro-ph](https://arxiv.org/abs/astro-ph)].
- [32] Jose María Ezquiaga and Miguel Zumalacárregui. “Gravitational wave lensing beyond general relativity: Birefringence, echoes, and shadows”. In: *Phys. Rev. D* 102 (12 Dec. 2020), p. 124048. DOI: [10.1103/PhysRevD.102.124048](https://doi.org/10.1103/PhysRevD.102.124048).
- [33] Ashish Kumar Meena and Jasjeet Singh Bagla. “Gravitational lensing of gravitational waves: wave nature and prospects for detection”. In: *Monthly Notices of the Royal Astronomical Society* 492.1 (Dec. 2019), pp. 1127–1134. ISSN: 0035-8711. DOI: [10.1093/mnras/stz3509](https://doi.org/10.1093/mnras/stz3509).
- [34] Irwin I. Shapiro. “Fourth Test of General Relativity”. In: *Phys. Rev. Lett.* 13 (26 Dec. 1964), pp. 789–791. DOI: [10.1103/PhysRevLett.13.789](https://doi.org/10.1103/PhysRevLett.13.789).
- [35] Ryuichi Takahashi and Takashi Nakamura. “Wave Effects in the Gravitational Lensing of Gravitational Waves from Chirping Binaries”. In: *The Astrophysical Journal* 595.2 (Oct. 2003), pp. 1039–1051. DOI: [10.1086/377430](https://doi.org/10.1086/377430). URL: <https://doi.org/10.1086/377430>.
- [36] A. Renske A. C. Wierda et al. *Beyond the detector horizon: Forecasting gravitational-wave strong lensing*. 2021. arXiv: [2106.06303](https://arxiv.org/abs/2106.06303) [[astro-ph](https://arxiv.org/abs/astro-ph).HE].

- [37] National Science Foundation. *Press release: Upgraded LIGO to search for universe's most extreme events*. URL: [https://www.nsf.gov/news/news\\_summ.jsp?cntn\\_id=297414](https://www.nsf.gov/news/news_summ.jsp?cntn_id=297414).
- [38] Rana X. Adhikari. "Gravitational radiation detection with laser interferometry". In: *Rev. Mod. Phys.* 86 (1 Feb. 2014), pp. 121–151. doi: [10.1103/RevModPhys.86.121](https://doi.org/10.1103/RevModPhys.86.121).
- [39] Jolien D. E. Creighton and Warren G. Anderson. *Gravitational-Wave Physics and Astronomy: An Introduction to Theory, Experiment and Data Analysis*. 1st ed. John Wiley & Sons, Incorporated, 2011. ISBN: 9783527408863.
- [40] J. Veitch and A. Vecchio. "Bayesian coherent analysis of in-spiral gravitational wave signals with a detector network". In: *Phys. Rev. D* 81 (6 Mar. 2010), p. 062003. doi: [10.1103/PhysRevD.81.062003](https://doi.org/10.1103/PhysRevD.81.062003).
- [41] John Skilling. "Nested Sampling". In: *AIP Conference Proceedings* 735.1 (2004), pp. 395–405. doi: [10.1063/1.1835238](https://doi.org/10.1063/1.1835238).
- [42] John Skilling. "Nested sampling for general Bayesian computation". In: *Bayesian Analysis* 1.4 (2006), pp. 833–859. doi: [10.1214/06-BA127](https://doi.org/10.1214/06-BA127).
- [43] B. P. Abbott et al. "Improved Analysis of GW150914 Using a Fully Spin-Precessing Waveform Model". In: *Phys. Rev. X* 6 (4 Oct. 2016), p. 041014. doi: [10.1103/PhysRevX.6.041014](https://doi.org/10.1103/PhysRevX.6.041014).
- [44] B. P. Abbott et al. "GW170817: Observation of Gravitational Waves from a Binary Neutron Star Inspiral". In: *Phys. Rev. Lett.* 119 (16 Oct. 2017), p. 161101. doi: [10.1103/PhysRevLett.119.161101](https://doi.org/10.1103/PhysRevLett.119.161101).
- [45] B. P. Abbott et al. *GWTC-2: Compact Binary Coalescences Observed by LIGO and Virgo During the First Half of the Third Observing Run*. 2021. arXiv: [2010.14527](https://arxiv.org/abs/2010.14527) [gr-qc].
- [46] Luciano Rezzolla, Elias R. Most and Lukas R. Weih. "Using Gravitational-wave Observations and Quasi-universal Relations to Constrain the Maximum Mass of Neutron Stars". In: *The Astrophysical Journal* 852.2 (Jan. 2018), p. L25. doi: [10.3847/2041-8213/aaa401](https://doi.org/10.3847/2041-8213/aaa401).
- [47] Todd A. Thompson et al. "A noninteracting low-mass black hole–giant star binary system". In: *Science* 366.6465 (2019), pp. 637–640. doi: [10.1126/science.aau4005](https://doi.org/10.1126/science.aau4005).
- [48] Buchner, J. et al. "X-ray spectral modelling of the AGN obscuring region in the CDFS: Bayesian model selection and catalogue". In: *A&A* 564 (2014), A125. doi: [10.1051/0004-6361/201322971](https://doi.org/10.1051/0004-6361/201322971). URL: <https://doi.org/10.1051/0004-6361/201322971>.



## A Appendix

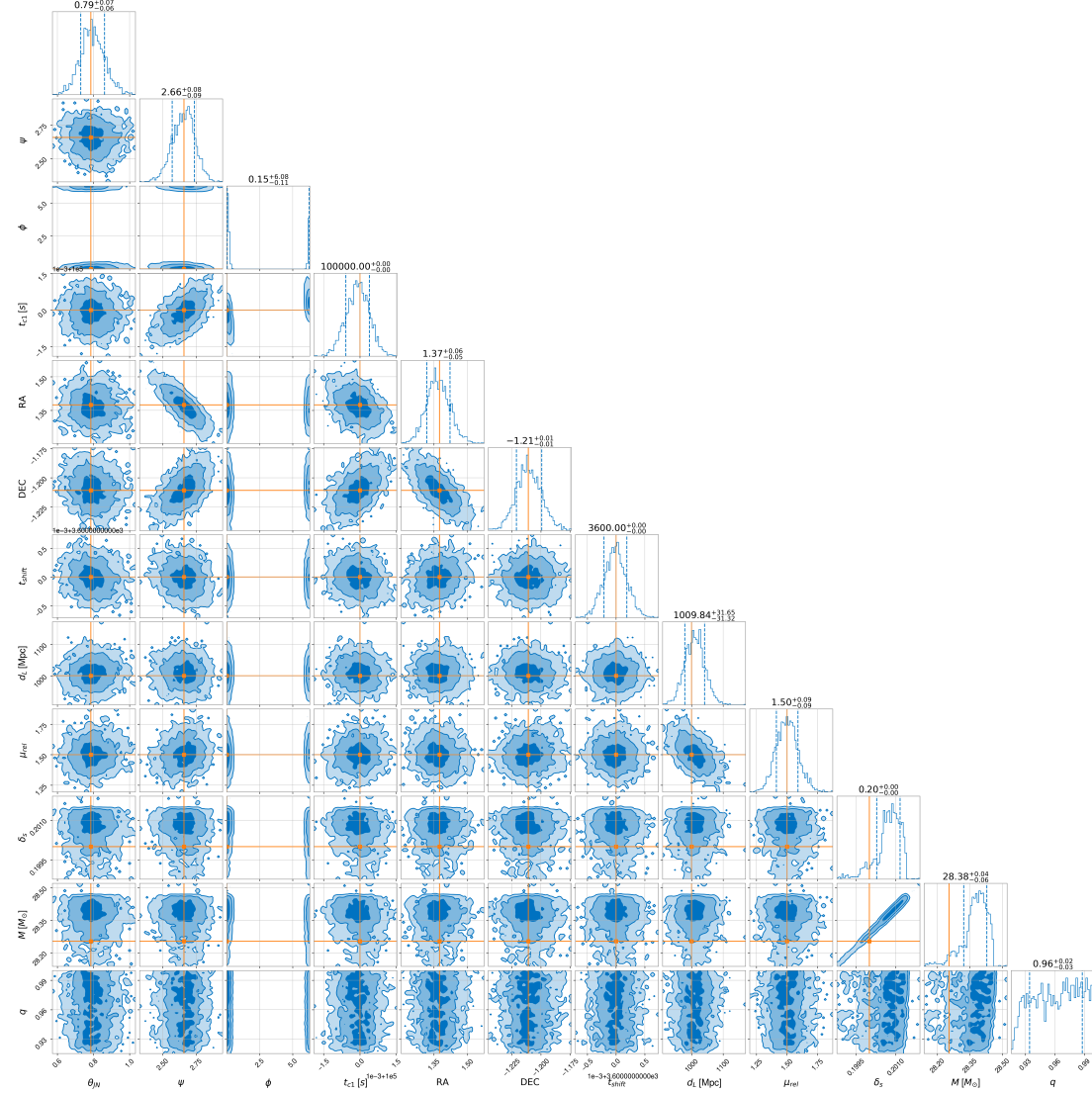


Figure 8: Example of a corner plot: the Lightman-Lee injected and Lightman-Lee returned wave of the BBH system. My excuses for the bad resolution, these images are simply too large to fit on a traditional page.